




# Optimal Energy Growth in Stably Stratified Turbulent Couette Flow

Grigory V. Zasko<sup>1,2</sup>  · Andrey V. Glazunov<sup>2</sup> · Evgeny V. Mortikov<sup>2,3</sup> · Yuri M. Nechepurenko<sup>1,2</sup> · Pavel A. Perezhogin<sup>2</sup>

Received: 30 August 2021 / Accepted: 22 August 2022 / Published online: 8 September 2022  
© The Author(s), under exclusive licence to Springer Nature B.V. 2022

## Abstract

Optimal disturbances of a turbulent stably stratified plane Couette flow in a wide range of Reynolds and Richardson numbers are studied. These disturbances are computed based on a simplified system of equations in which turbulent Reynolds stresses and heat fluxes are approximated by isotropic viscosity and diffusivity with the coefficients obtained from results of direct numerical simulation. Three types of disturbances are considered: large-scale streamwise-elongated rolls converting into streamwise streaks; large-scale vortical structures, inclined in the vertical plane, changing the inclination to the opposite in process of their evolution; near-wall rolls converting into streaks. Large-scale rolls and streaks predominate at neutral or weakly stable stratification while the inclined structures begin to dominate at moderately stable stratification. Near-wall rolls and streaks appear at any stratification and their spanwise size in wall length units does not depend on the values of Reynolds and Richardson numbers. It is shown that the development of inclined optimal disturbances is due to the coupled action of the lift-up effect and the inviscid Orr mechanism. The energetics of the optimal disturbances is discussed. It is shown that inclined optimal disturbances dissipate rapidly after reaching maximum energy amplification.

**Keywords** Atmospheric boundary layer · Large-scale structures · Near-wall structures · Optimal disturbances · Stably stratified turbulence

## 1 Introduction

Organized structures such as elongated counter-rotating rolls with axes of rotation directed along the mean flow and streamwise velocity streaks are common in wall-bounded neutrally

---

✉ Grigory V. Zasko  
zasko.gr@bk.ru

<sup>1</sup> Keldysh Institute of Applied Mathematics, Russian Academy of Sciences, Miusskaya sq., 4, Moscow, Russia 125047

<sup>2</sup> Marchuk Institute of Numerical Mathematics, Russian Academy of Sciences, Gubkin str., 8, Moscow, Russia 119333

<sup>3</sup> Research Computing Center of Lomonosov Moscow State University, Leninskie Gory str., 1, p. 4, Moscow, Russia 119991

stratified turbulent shear flows. The rolls transform to the streaks due to the lift-up effect (Ellingsen and Palm 1975; Landahl 1980), see also review Brandt (2014). This effect is accompanied by conversion of mean flow kinetic energy into the kinetic energy of streamwise velocity fluctuations, which significantly increases the energy of the streaks in comparison with the energy of the rolls that produce them. The size of the streaks in the spanwise and wall-normal directions varies in a wide range, from values comparable to the thicknesses of the viscous and buffer layers (Kline et al. 1967; Smith and Metzler 1983; Moin and Kim 1982) to values of the same order as the thicknesses of the logarithmic and outer layers (see review Cossu and Hwang 2017). For the turbulent plane Couette flow, organized structures with spanwise and wall-normal scales close to the channel height were first obtained numerically in Lee and Kim (1991) and Komminaho et al. (1996), and later confirmed by laboratory measurements (Kitoh et al. 2005). These structures are sometimes referred to as “very large structures” or “superstructures”. The secondary instability and nonlinear effects allow a “rolls-streaks-rolls” regeneration cycle and self-sustainment of these structures within the turbulent flow (Hamilton et al. 1995; Waleffe 1997). This, apparently, explains the fact that streaks account for a significant part of the streamwise velocity variance in wall-bounded flows. It was shown in Rawat et al. (2015) that the regeneration cycle is not associated with non-linear interactions of the organized structures with small-scale turbulence.

The other organized structures observed in neutrally stratified turbulent boundary layers and wall-bounded turbulent flows are the hairpin vortices (Adrian 2007). The large-scale hairpin vortices were also observed in the atmospheric boundary layer (Homemma and Adrian 2003). However, for the turbulent plane Couette flow, recent direct numerical simulations at high Reynolds number (Mortikov et al. 2019) or in very large computational domain (Lee and Moser 2018) do not show the presence of the large-scale hairpin vortices, while the large-scale streamwise-elongated rolls and streaks are observed and contribute significantly to the momentum flux near the channel centre.

Steady-state turbulent wall-bounded flows in many cases have linearly stable mean velocity profiles (Malkus 1956; Bakewell and Lumley 1967). For such flows, instead of analysing their linear instability, it is of interest to study their non-modal stability, i.e. to search for disturbances that maximize their energy on finite time intervals (Butler and Farrell 1992; Reddy and Henningson 1993; Schmid and Henningson 1994). These disturbances are usually called optimal disturbances or optimal perturbations (Schmid and Henningson 2001; Schmid 2007). The existence of such disturbances is associated with the non-orthogonality of the eigenmodes of the disturbance evolution equations linearised with respect to the main flow. Optimal disturbances were originally discovered and investigated for canonical laminar flows (see Schmid and Henningson 2001). They are widely used to explain the bypass laminar–turbulent transition (see Boiko et al. (2011) and references therein). In Foster (1997), they have also been used to analyse large-scale structures in the laminar Ekman layer, which is the simplest model of the atmospheric boundary layer.

Optimal disturbances of turbulent flows were first computed in del Alamo and Jimenez (2006), Pujals et al. (2009) (turbulent Poiseuille flow) and in Cossu et al. (2009) (zero-pressure-gradient turbulent boundary layer). Optimal responses of the turbulent neutrally stratified plane Couette flow to initial conditions and harmonic (or stochastic) forcing were obtained in Hwang and Cossu (2010). Two types of high-energy coherent structures were obtained: near-wall streaks with characteristic spanwise and wall-normal sizes of about 80–100 (in dimensionless length wall units) and large-scale streaks with a spanwise size exceeding the height of the entire turbulent boundary layer. These results are in qualitative and quantitative agreement with the experimental observations and the numerical simulations.

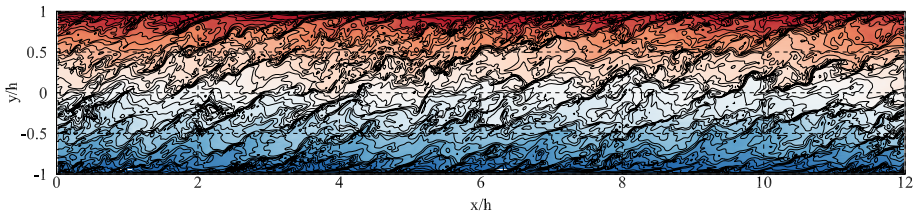


**Fig. 1** Snapshot of temperature isolines in vertical cross-section of a stably-stratified turbulent plane Couette flow ( $h$  is channel half-height,  $y$  is wall-normal direction, and  $x$  is streamwise direction) from the DNS results of Glazunov et al. (2019) at Reynolds number  $Re = 4 \times 10^4$  and Richardson number  $Ri = 0.03$

For all considered neutrally stratified wall-bounded turbulent flows with zero spanwise mean velocity, the optimal energy growth is achieved for disturbances with zero streamwise wavenumber. Such disturbances develop into streamwise streaks due to the lift-up effect. On the other hand, according to the results of direct numerical simulation (DNS) and large-eddy simulation (LES) (Sullivan et al. 2016; Glazunov et al. 2019), there are large-scale organized structures with non-zero values of the streamwise wavenumber, which arise in stably stratified conditions. The existence of such structures is indirectly confirmed by field measurements in the stable atmospheric boundary layer (Sullivan et al. 2016; Glazunov et al. 2019; Petenko et al. 2019). These structures manifest themselves in the instantaneous temperature fields, where they appear as irregular inclined thin layers with large gradients (fronts), spaced from each other by distances comparable to the height of the entire turbulent layer and separated by well-mixed regions. The presence of these structures is indicated by non-zero skewness in the distribution of the gradients of temperature fluctuations (Sullivan et al. 2016; Glazunov et al. 2019).

In Sullivan et al. (2016), a vortex structure associated with the observed temperature fronts was extracted from LES data (see Fig. 18 in Sullivan et al. 2016), using conditional averaging and vortex visualization method. The spatial configuration and the mechanisms responsible for the emergence of such structures have not yet been explained.

Note that the formation of such inclined structures was found for the stably stratified Ekman layer (LES, Sullivan et al. (2016)) as well as plane Couette flow (DNS and LES, Glazunov et al. (2019), see Fig. 1, where the isolines of the temperature field are shown, and the fronts correspond to regions of their larger concentration). In addition, similar structures were observed in a stably stratified channel flow above an urban-like surface (LES, Glazunov (2014)). These findings underline the importance of stable stratification in their formation and a lesser influence of the effects due to rotation in the Ekman spiral or due to peculiarities of the near-wall turbulence. The presence of such inclined structures might have a significant impact on the dynamics of stably stratified turbulence. In particular, S.S. Zilitinkevich in Glazunov et al. (2019) suggested that these structures can be responsible for growth of the turbulent Prandtl number with increasing the gradient Richardson number (see Zilitinkevich et al. 2007, 2013, and references therein).

Optimal disturbances of a turbulent stably stratified plane Couette flow were first computed in Zasko et al. (2020). In that paper, the total energy functional included the available potential energy of buoyancy perturbations in addition to the disturbance kinetic energy. Mean velocity and mean temperature, as well as effective coefficients of eddy viscosity and eddy diffusivity were obtained from the DNS results (Mortikov et al. 2019; Glazunov et al. 2019). It was shown that the form of optimal disturbances changes with the increase in stability, i.e. the streamwise-elongated structures are replaced with the large-scale inclined structures with a

non-zero streamwise wavenumber. Analysing the instantaneous fluctuation fields from the DNS, where the large-scale inclined temperature fronts are observed (as in Fig. 1), it was shown in Zasko et al. (2020) that high-energy large-scale Fourier harmonics significantly correlate with the optimal disturbances. Spatial scales of the high-energy Fourier harmonics also coincide with those of the optimal disturbances. In Zasko and Nechepurenko (2021), it was found that the optimal disturbances significantly differ from the least stable eigenmodes of the linearised system and represent a linear combination of a large number of essentially non-orthogonal eigenmodes.

Previously, optimal disturbances with non-zero streamwise wavenumber were obtained by Butler and Farrell (1992) for the laminar neutrally stratified Couette flow at low Reynolds numbers. The coupled action of two mechanisms was proposed to explain the formation of these disturbances and the growth of their energy, namely, the lift-up effect (in that work it was referred to as the vortex-tilting mechanism) and the inviscid Orr mechanism (Orr 1907; Schmid and Henningson 2001), which in Butler and Farrell (1992) was referred to as 2D Reynolds stress effect. The impact of the Orr mechanism increases for disturbances with short growth time. In the recent paper Jiao et al. (2021), these mechanisms were studied in more detail to describe the "oblique" and "streak" types of laminar–turbulent transition in a neutrally stratified plane Couette flow. Inclined optimal disturbances with a non-zero streamwise wavenumber were also found in Kaminski et al. (2014, 2017) for a stably stratified free shear flow.

In this paper, we consider a turbulent stably stratified plane Couette flow in a much wider range of values of the Richardson and Reynolds numbers than in Zasko et al. (2020). For the large-scale disturbances, we separate the two above-mentioned mechanisms of energy growth and analyse the energy balance of disturbances during the period of their development. A qualitative explanation of the predominance of inclined structures in the stably stratified turbulent Couette flow is proposed. In addition, we consider small-scale local suboptimal disturbances resembling near-wall rolls developing into near-wall streaks and demonstrate a weak dependence of their spatial structure on the Richardson number.

An often used approach for determining optimal disturbances in turbulent flows is to consider a modified system of Navier–Stokes equations with an isotropic effective viscosity including both molecular and turbulent components (Reynolds and Hussain 1972). The scalar viscosity coefficient is found in such a way that the mean turbulent flow is a stationary solution to the simplified problem under the same boundary conditions and external forcing. In plane-parallel flows, such as Couette flow or Poiseuille flow, this coefficient can be found either from the DNS data (as the ratio of the vertical total momentum flux to gradient of the mean streamwise velocity, see Hwang and Cossu 2010) or using semi-empirical and analytical approximations consistent with available measurement data and DNS.

It is worth noting that this approach is a rather rough approximation of the non-linear interactions of large-scale disturbances with small-scale turbulence, since it does not take into account the possible non-locality and anisotropy of turbulent transport (see, e.g., McKeon 2017, where this issue is discussed). Another disadvantage of this approach is that the eddy viscosity includes a part associated with the transfer of momentum by the sought optimal disturbances themselves. This might influence the quantitative results in flows which contain large-scale organized structures of significant magnitude. For example, in a neutrally stratified turbulent Couette flow at high Reynolds numbers, about 20–30% of the momentum flux in the channel centre is due to rolls (Mortikov et al. 2019). In particular, this could be the reason for the rather low amplification of the optimal disturbances obtained in Hwang and Cossu (2010), and similar results presented below for neutral and close to neutral stratification. However, the large vortical structures play a noticeably smaller role in the transfer



of momentum (and heat) under the stable stratification comparing to neutral one. Another important argument in favour of the applicability of the diffusion approximation in the considered problem is that, in some cases under stable stratification, the terms approximating the Reynolds stresses and turbulent heat fluxes begin to play an appreciable role in the balance of the disturbance energy only at times exceeding the maximum amplification time. This effect will be discussed below when analysing the energy cycle of large-scale disturbances, which appear as inclined structures. In addition, stable stratification damps the spatial scales of turbulent eddies, limiting their characteristic size in proportion to the Obukhov length. This leads to the separation of the spatial and temporal turbulent scales and the scales of the considered disturbances (at least at the initial stages of their development), thus allowing to consider turbulent transport as a diffusion process. Based on the foregoing, we assume that the proposed approach may allow one to correctly determine the dependence of the type of the flow disturbances on the parameters representing the stable stratification. In addition to the turbulent viscosity approximation, we use isotropic scalar effective diffusivity to parameterise the sum of molecular and turbulent heat fluxes.

To compute the optimal disturbances in this work, we use the novel numerical technology based on spatial approximation by the Galerkin–collocation method (Zasko et al. 2020), projection onto the subspace of non-divergent grid functions (Nechepurenko 2012), and efficient algorithm for computing the maximum of the matrix exponential norm (Nechepurenko and Sadkane 2011).

The paper is organized as follows: in Sect. 2 we briefly introduce the mathematical problem to be solved and numerical technology which we use for computing the optimal disturbances. The results related to the large-scale structures are reported in Sect. 3. The physical mechanisms are discussed in Sect. 4. The results related to the near-wall structures are presented in Sect. 5. Section 6 summarizes the paper.

Throughout this paper,  $\|\cdot\|_2$  denotes the 2-norm for vectors and matrices, and superscripts  $T$  and  $*$  denote the symbols of transposition and conjugate transposition, respectively.

## 2 Background

Consider the motion of a viscous incompressible fluid in a gravity field in an infinite three-dimensional channel of half-height  $h$ :  $-h < y < h$ , where  $x$  (streamwise),  $y$  (wall-normal), and  $z$  (spanwise) are Cartesian coordinates. The upper wall of the channel moves with the velocity  $(U_0/2, 0, 0)$ , the lower one moves with the velocity  $(-U_0/2, 0, 0)$ , temperatures  $T_2 > T_1$  are maintained on the walls, respectively, and the velocity satisfies the no-slip condition. The fluid motion in the Boussinesq approximation is governed by Navier–Stokes, continuity, and heat transfer equations, expressed in dimensionless variables as:

$$\begin{aligned} \frac{\partial \mathbf{u}}{\partial t} + (\mathbf{u} \cdot \nabla) \mathbf{u} + \nabla p - \frac{1}{Re} \Delta \mathbf{u} - (0, Ri T, 0)^T &= 0, \\ \frac{\partial T}{\partial t} + (\mathbf{u} \cdot \nabla) T - \frac{1}{Pr Re} \Delta T &= 0, \\ \nabla \cdot \mathbf{u} &= 0, \end{aligned} \tag{1}$$

where  $\nabla = (\partial/\partial x, \partial/\partial y, \partial/\partial z)^T$  is the nabla operator and  $\Delta = \nabla \cdot \nabla$  is the Laplace operator. Here  $\mathbf{u} = (U, V, W)^T$ ,  $p$ , and  $T$  are dimensionless components of the velocity vector (in the directions of  $x$ ,  $y$ , and  $z$ ), the specific pressure and temperature, respectively;  $Re = U_0 h / \nu$ ,  $Ri = g(T_2 - T_1) h / (T_1 U_0^2)$ , and  $Pr = \nu / \mu$  are Reynolds, Richardson, and Prandtl numbers,

$\nu$  is the kinematic viscosity,  $\mu$  is the thermal diffusivity, and  $g$  is the acceleration due to gravity. The fluid temperature  $T$  at the upper ( $y = 1$ ) and lower ( $y = -1$ ) walls are 2 and 1, respectively. The walls move at the speeds of  $1/2$  and  $-1/2$  in the streamwise direction.

Direct numerical simulation of (1) was performed in Mortikov et al. (2019) and Glazunov et al. (2019) in the computational domain with sizes  $L_x = 12, L_y = 2, L_z = 8$ . Periodic boundary conditions in the directions of  $x$  and  $z$  were assumed for velocity and temperature. The computations were carried out for the fixed Prandtl number  $Pr = 0.7$  and Reynolds and Richardson numbers lying within the ranges  $1 \leq Re \times 10^{-4} \leq 6$  and  $0 \leq Ri \leq 0.06$ . To compute the profiles of the mean turbulent flow, averaging (denoted by  $\bar{(\cdot)}$ ) was made over the horizontal coordinates and time in a sufficiently large part of the model trajectory after reaching a quasi-equilibrium state by the turbulent flow. The mean values of the streamwise velocity and temperature are denoted by  $\bar{U} = \bar{U}(y)$  and  $\bar{T} = \bar{T}(y)$ , respectively. The mean values of the other velocity components on sufficiently large time intervals turned out to be negligible and we consider them equal to zero.

The mean values of total dimensionless momentum and heat fluxes are also obtained from DNS data and are defined as:

$$\tau = \overline{UV} - \frac{1}{Re} \frac{d\bar{U}}{dy} = \text{const}, \quad F_T = \overline{TV} - \frac{1}{Pr Re} \frac{d\bar{T}}{dy} = \text{const}.$$

Following del Alamo and Jimenez (2006), Pujals et al. (2009), Cossu et al. (2009), Hwang and Cossu (2010), and Zasko et al. (2020), we assume that the evolution of large-scale flow is described by the following system of equations (Unsteady RANS):

$$\begin{aligned} \frac{\partial \tilde{\mathbf{u}}}{\partial t} + (\tilde{\mathbf{u}} \cdot \nabla) \tilde{\mathbf{u}} + \nabla \tilde{p} - \Delta_\nu \tilde{\mathbf{u}} - (0, Ri \tilde{T}, 0)^T &= 0, \\ \frac{\partial \tilde{T}}{\partial t} + (\tilde{\mathbf{u}} \cdot \nabla) \tilde{T} - \Delta_\mu \tilde{T} &= 0, \\ \nabla \cdot \tilde{\mathbf{u}} &= 0, \end{aligned} \tag{2}$$

where

$$\Delta_\nu = \bar{\nu} \frac{\partial^2}{\partial x^2} + \frac{\partial}{\partial y} \bar{\nu} \frac{\partial}{\partial y} + \bar{\nu} \frac{\partial^2}{\partial z^2}, \quad \Delta_\mu = \bar{\mu} \frac{\partial^2}{\partial x^2} + \frac{\partial}{\partial y} \bar{\mu} \frac{\partial}{\partial y} + \bar{\mu} \frac{\partial^2}{\partial z^2},$$

with the operator  $\Delta_\nu$  acting on the velocity vector component-wise,  $\tilde{\cdot}$  denoting the Reynolds averaging operator, and the modified pressure  $\tilde{p}$  excluding the isotropic part of the Reynolds stress. The interaction with small-scale turbulence is approximated by isotropic eddy viscosity and isotropic eddy diffusivity with coefficients depending only on the wall-normal coordinate:

$$\bar{\nu}(y) = -\tau / \left( \frac{d\bar{U}}{dy} \right), \quad \bar{\mu}(y) = -F_T / \left( \frac{d\bar{T}}{dy} \right).$$

The eddy viscosity and the eddy diffusivity are equal to their molecular values ( $1/Re$  and  $1/Pr Re$ ) at the channel walls.

Profiles  $\bar{U}(y), \bar{T}(y)$  of the mean turbulent flow and coefficients of the eddy viscosity  $\bar{\nu}(y)$  and eddy diffusivity  $\bar{\mu}(y)$  are shown in Fig. 2a–d at various Reynolds and Richardson numbers ranging from the case of neutral stratification ( $Ri = 0$ ), where the temperature is considered as a passive scalar, to the strongly stratified case ( $Ri = 0.055$ ). With increasing Richardson number, stable stratification damps the turbulent mixing, limiting the characteristic spatial scales of the turbulent eddies, which leads to the gradual decrease in the eddy viscosity and diffusivity. The profiles of the mean velocity and temperature near the channel centre tend to be linear with increasing Richardson number, and their mean gradient increases.

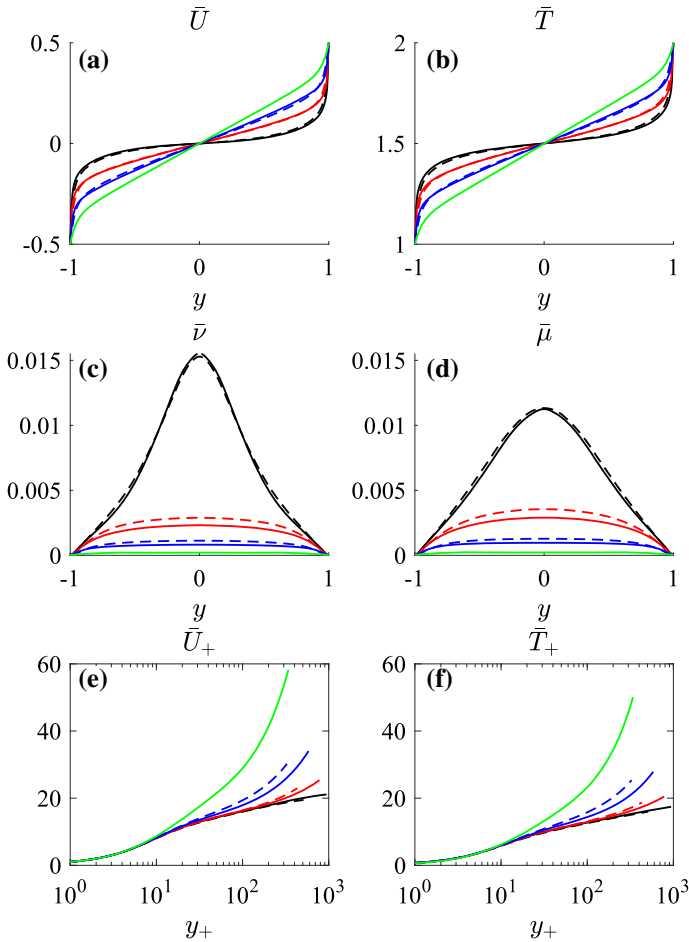


**Fig. 2** Profiles  $\bar{U}(y)$ ,  $\bar{T}(y)$ ,  $\bar{v}(y)$ ,  $\bar{\mu}(y)$ ,  $\bar{U}_+(y_+)$ , and  $\bar{T}_+(y_+)$  (a-e) of the mean flow at  $Re = 2 \times 10^4$  (dotted),  $Re = 4 \times 10^4$  (solid) and  $Ri = 0$  (black),  $Ri = 0.01$  (red), and  $Ri = 0.03$  (blue). The green lines indicate the profiles at  $Re = 4 \times 10^4$  and  $Ri = 0.055$ . The profiles of  $\bar{U}_+(y_+)$ ,  $\bar{T}_+(y_+)$  are shown only for the lower half-channel

Dynamic features of turbulent flow are characterized by the friction velocity  $u_* = \sqrt{|\tau_0|/\rho}$  and the friction Reynolds number  $Re_\tau = u_* Re/U_0$ , where  $\tau_0$  is the dimensional momentum flux and  $\rho$  is the fluid density. The turbulent temperature scale is  $T_* = |F_{T_0}|/u_*$ , where  $F_{T_0}$  is the dimensional heat flux. We use the subscript “+” for the variables non-dimensionalised by turbulent scales:

$$y_+ = Re_\tau (y + 1), \quad \bar{U}_+ = Re_\tau (\bar{U} + 0.5), \quad \bar{T}_+ = \frac{T_1}{T_*} (\bar{T} - 1),$$

which are shifted to be equal zero at the lower wall. Figure 2e-f shows the profiles  $\bar{U}_+(y_+)$ ,  $\bar{T}_+(y_+)$  of the mean turbulent flow at the lower half-channel at various Reynolds and Richardson numbers. The profiles coincide in the viscous sublayer (approximately, for  $y_+ \leq 10$ ), which indicates that the DNS was carried out with sufficient grid resolution. The logarithmic

layer is pronounced at neutral and weakly stable stratification, while at moderately stable stratification the influence of buoyancy forces starts from the buffer layer.

Stably stratified turbulence is characterized by the Obukhov length scale  $L = u_*^2 T_1 / (g T_*)$ . It is worth noting that we define  $L$  without the additional multiplicative factor  $1/\kappa$ , where  $\kappa$  is the von Kármán’s constant, to keep the same notation as in Glazunov et al. (2019), where the DNS results of the considered flow are presented. This length scale was proposed by Obukhov (1971) and is used in the Monin–Obukhov similarity theory (Monin and Obukhov 1954) to express the statistical features of turbulence in the atmospheric boundary layer. The dimensionless parameter  $\zeta = h/L$ , which we call the stability parameter, universally characterizes stratified turbulence (with the exception of thin near-wall layer) in the considered flow at very high Reynolds numbers.

Values of the friction Reynolds number  $Re_\tau$  and the stability parameter  $\zeta$  for all considered pairs of  $(Re, Ri)$  are presented in Table 1.

### 2.1 Linear Model

By construction, system (2) has the following stationary solution:

$$\tilde{\mathbf{u}} = \bar{\mathbf{u}} \equiv (\bar{U}(y), 0, 0)^T, \quad \tilde{p} = \bar{P}(y), \quad \tilde{T} = \bar{T}(y),$$

with profiles of streamwise velocity, pressure, and temperature satisfying the relations:

$$-\bar{v} \frac{d\bar{U}}{dy} = \tau, \quad -\bar{\mu} \frac{d\bar{T}}{dy} = F_T, \quad \frac{d\bar{P}}{dy} = Ri \bar{T}.$$

This flow is referred to as a main flow.

Represent an arbitrary solution of the system (2) in the neighbourhood of the main flow as follows:

$$(\tilde{\mathbf{u}}, \tilde{p}, \tilde{T}) = (\bar{\mathbf{u}}, \bar{P}, \bar{T}) + \varepsilon(\mathbf{u}', p', T') + o(\varepsilon), \tag{3}$$

where  $\mathbf{u}' = (u', v', w')$  and  $\varepsilon$  is a small parameter. Requiring that (3) satisfies system (2) for any arbitrarily small absolute value of  $\varepsilon$ , the following linearised equations for the evolution of small disturbances are obtained:

$$\begin{aligned} \frac{\partial \mathbf{u}'}{\partial t} + \bar{U} \frac{\partial \mathbf{u}'}{\partial x} + \left( \frac{d\bar{U}}{dy} v', -Ri T', 0 \right)^T + \nabla p' - \Delta_\nu \mathbf{u}' &= 0, \\ \frac{\partial T'}{\partial t} + \bar{U} \frac{\partial T'}{\partial x} + \frac{d\bar{T}}{dy} v' - \Delta_\mu T' &= 0, \\ \nabla \cdot \mathbf{u}' &= 0. \end{aligned} \tag{4}$$

Equations (4) are considered with zero boundary conditions for  $u', v', w'$ , and  $T'$  on the channel walls.

We seek for the solutions of system (4), periodic in streamwise and spanwise directions, which gain the maximum growth of the disturbance total energy density:

$$\frac{1}{8l_x l_z} \int_{-l_x}^{l_x} \int_{-1}^1 \int_{-l_z}^{l_z} \left( u'^2 + v'^2 + w'^2 + \frac{Ri}{d\bar{T}/dy} T'^2 \right) dx dy dz,$$

where  $l_x$  and  $l_z$  are the half-periods of the disturbance in  $x$  and  $z$  directions, respectively. Since the main flow is independent on  $x$  and  $z$ , any periodic in  $x$  and  $z$  solution  $(u', v', w', p', T')$

**Table 1** Values of  $\Gamma_{\max}$ ,  $(\alpha_{\text{opt}}, \gamma_{\text{opt}})$ , and  $t_{\text{opt}}$  for the large-scale optimal disturbances, values of  $\tilde{\Gamma}_{\max}$ ,  $\tilde{\gamma}_{\text{opt}}$ , and  $\tilde{t}_{\text{opt}}$  for the near-wall disturbances, and flow parameters  $\zeta$  and  $Re_{\tau}$  at various values of  $Ri$  and  $Re$

$Ri \times 10^2$	$Re \times 10^{-4}$	$\Gamma_{\max}$	$(\alpha_{\text{opt}}, \gamma_{\text{opt}})$	$t_{\text{opt}}$	$\zeta$	$Re_{\tau}$	$\tilde{\Gamma}_{\max}$	$\tilde{\gamma}_{\text{opt}}$	$\tilde{t}_{\text{opt}}$
0	0.075*	3.31*	(0.00, 1.46)*	—	0	—	—	—	—
	1	2.44	(0.00, 1.20)	41.9	0	276	2.72	17.4	2.49
	2	2.31	(0.00, 1.15)	46.7	0	513	2.68	32.3	1.43
	4	2.26	(0.00, 1.14)	50.8	0	947	2.81	63.6	0.80
0.5	1	11.7	(0.00, 1.00)	121	0.24	252	2.78	15.9	3.03
	2	15.0	(0.00, 0.94)	148	0.27	463	2.76	28.7	1.79
	4	21.0	(0.00, 0.91)	171	0.29	843	2.88	56.1	1.03
1	1	18.2	(0.00, 0.99)	108	0.52	236	3.06	14.9	3.68
	2	22.2	(0.00, 0.94)	122	0.57	434	2.90	25.0	2.26
	4	28.3	(0.00, 0.92)	131	0.63	786	2.93	51.5	1.21
2	1	22.9	(0.00, 1.06)	74.4	1.19	205	4.41	12.9	5.95
	2	24.8	(0.00, 1.00)	81.2	1.27	383	3.44	22.9	3.10
	4	30.4	(0.00, 1.01)	80.5	1.46	679	3.17	39.8	1.89
3	1	25.2	(0.00, 1.23)	52.3	2.15	168	8.90	10.6	11.04
	2	24.8	(0.00, 1.12)	57.5	2.17	330	4.67	20.8	4.63
	4	30.4	(0.39, 1.16)	46.6	2.50	586	3.77	33.9	2.84
	6	38.1	(0.47, 1.14)	46.7	2.89	782	3.63	45.7	2.34
3.25	1	27.8	(0.31, 1.33)	41.6	2.64	151	13.1	9.50	14.3
3.5	1	29.4	(0.40, 1.37)	38.9	3.05	140	17.6	8.81	16.4
4	2	28.6	(0.50, 1.18)	40.1	3.46	271	8.93	15.6	9.2
	4	36.1	(0.57, 1.10)	41.8	3.81	500	5.03	31.5	4.1
	6	46.7	(0.60, 1.05)	44.1	4.44	664	4.81	41.8	3.5
4.5	2	35.3	(0.61, 1.15)	39.7	4.64	228	15.2	14.4	12.5
	4	40.1	(0.63, 1.06)	41.4	4.64	456	6.37	28.7	5.4
	6	50.5	(0.65, 1.02)	43.7	5.32	612	5.82	38.6	4.4
4.75	2	48.9	(0.69, 1.07)	41.7	5.88	195	21.7	12.3	15.5
5	4	45.5	(0.68, 1.02)	41.6	5.69	409	8.65	25.8	7.3
5.5	4	56.1	(0.73, 0.97)	43.8	7.46	342	15.2	21.5	10.9

The superscript "\*" marks data from Hwang and Cossu (2009)

of the system (4) can be expanded in a series of solutions having the form:

$$(u_{\alpha\gamma}, v_{\alpha\gamma}, w_{\alpha\gamma}, p_{\alpha\gamma}, T_{\alpha\gamma})e^{i\alpha x + i\gamma z}, \tag{5}$$

where  $\alpha, \gamma$  are streamwise and spanwise wavenumbers respectively, while  $u_{\alpha\gamma}, v_{\alpha\gamma}, w_{\alpha\gamma}, p_{\alpha\gamma}$ , and  $T_{\alpha\gamma}$  are complex amplitudes depending only on  $y$  and  $t$ . It can be shown that the maximum growth of the disturbance total energy density is attained for solutions of the form (5). Thus, we can restrict ourselves to considering only such solutions. Note that, to obtain the physical quantities from the solution of the form (5), the real part should be taken. Substituting disturbance of the form (5) to (4), the following equations with respect

to disturbance amplitudes are obtained:

$$\begin{aligned}
 \frac{\partial u_{\alpha\gamma}}{\partial t} + i\alpha\bar{U}u_{\alpha\gamma} + \frac{d\bar{U}}{dy}v_{\alpha\gamma} + i\alpha p_{\alpha\gamma} - \Delta_v^{\alpha\gamma}u_{\alpha\gamma} &= 0, \\
 \frac{\partial v_{\alpha\gamma}}{\partial t} + i\alpha\bar{U}v_{\alpha\gamma} + \frac{\partial p_{\alpha\gamma}}{\partial y} - \Delta_v^{\alpha\gamma}v_{\alpha\gamma} - RiT_{\alpha\gamma} &= 0, \\
 \frac{\partial w_{\alpha\gamma}}{\partial t} + i\alpha\bar{U}w_{\alpha\gamma} + i\gamma p_{\alpha\gamma} - \Delta_v^{\alpha\gamma}w_{\alpha\gamma} &= 0, \\
 \frac{\partial T_{\alpha\gamma}}{\partial t} + i\alpha\bar{U}T_{\alpha\gamma} + \frac{d\bar{T}}{dy}v_{\alpha\gamma} - \Delta_\mu^{\alpha\gamma}T_{\alpha\gamma} &= 0, \\
 i\alpha u_{\alpha\gamma} + \frac{\partial v_{\alpha\gamma}}{\partial y} + i\gamma w_{\alpha\gamma} &= 0,
 \end{aligned}
 \tag{6}$$

where:

$$\Delta_v^{\alpha\gamma} = -\alpha^2\bar{v} + \frac{\partial}{\partial y}\bar{v}\frac{\partial}{\partial y} - \gamma^2\bar{v}, \quad \Delta_\mu^{\alpha\gamma} = -\alpha^2\bar{\mu} + \frac{\partial}{\partial y}\bar{\mu}\frac{\partial}{\partial y} - \gamma^2\bar{\mu}.
 \tag{7}$$

For a disturbance of the form (5) at time  $t$ , the total energy density is the sum of kinetic and potential components:

$$\mathcal{E}_t = \frac{1}{2} \int_{-1}^1 \left( |u_{\alpha\gamma}|^2 + |v_{\alpha\gamma}|^2 + |w_{\alpha\gamma}|^2 + \frac{Ri}{d\bar{T}/dy} |T_{\alpha\gamma}|^2 \right) dy.
 \tag{8}$$

The potential energy density is defined by analogy with the available potential energy of the stably stratified atmosphere (Lorenz 1955). The same functional was used in Kaminski et al. (2014, 2017) to study the optimal disturbances of strongly stratified shear layers.

The maximum growth

$$\Gamma^{\alpha\gamma}(t) = \max \frac{\mathcal{E}_t}{\mathcal{E}_0}
 \tag{9}$$

of the disturbance total energy density, where maximum is taken over all solutions of the system (6), is defined at fixed values of  $\alpha$ ,  $\gamma$ , and  $t$ .

Let us introduce the following notation:

$$\Gamma_{\max}^{\alpha\gamma} = \max_{t \geq 0} \Gamma^{\alpha\gamma}(t), \quad \Gamma_{\max} = \max_{\alpha, \gamma} \Gamma_{\max}^{\alpha\gamma}, \quad (\alpha_{\text{opt}}, \gamma_{\text{opt}}, t_{\text{opt}}) = \arg \max_{\alpha, \gamma, t} \Gamma^{\alpha\gamma}(t).
 \tag{10}$$

for maximum energy amplification (at fixed values of wavenumbers), global maximum energy amplification, optimal wavenumbers, and optimal time, respectively. Initial disturbance, at which  $\Gamma_{\max}$  is attained, is called the optimal disturbance.

### 2.2 Technology of Optimal Disturbance Computation

To compute the optimal disturbances, we use the technology developed in Zasko et al. (2020). After discretizing the system of Eq. (6) by the Galerkin–collocation method on the Gauss-Lobatto grid (see Canuto et al. 2007), we obtain a system of ordinary differential and algebraic equations of the form:

$$\frac{d\mathbf{q}}{dt} = \mathbf{J}\mathbf{q} - \mathbf{G}\mathbf{p}, \quad \mathbf{F}\mathbf{q} = 0
 \tag{11}$$

for  $\mathbf{q} = \mathbf{E}^{1/2}(\mathbf{u}^T, \mathbf{v}^T, \mathbf{w}^T, \mathbf{T}^T)^T$  and  $\mathbf{p}$ , where  $\mathbf{u}$ ,  $\mathbf{v}$ ,  $\mathbf{w}$ ,  $\mathbf{p}$ , and  $\mathbf{T}$  are  $n$ -component columns depending only on  $t$  with components being values of the amplitudes  $u_{\alpha\gamma}$ ,  $v_{\alpha\gamma}$ ,  $w_{\alpha\gamma}$ ,  $p_{\alpha\gamma}$ ,



$T_{\alpha\gamma}$  at the internal nodes of the computational grid, where  $n$  is the number of internal nodes. Here  $\mathbf{E}$  is a diagonal matrix of order  $4n$ , which is chosen such that the squared second norm  $\|\mathbf{q}\|_2^2$  be a discrete analog of the functional (7) of the disturbance total energy density. A detailed description of the spatial approximation and the matrices in (11) is given in Zasko et al. (2020). As it follows from the second equation of (11), the solution  $\mathbf{q}$  belongs to the kernel of  $\mathbf{F}$ . Defining  $\mathbf{q} = \mathbf{V}\boldsymbol{\varphi}$ , where  $\mathbf{V}$  is a rectangular matrix whose columns form an orthonormal basis in the kernel of  $\mathbf{F}$ , and multiplying the resulting equation on the left by  $\mathbf{V}^*$ , and also taking into account that  $\mathbf{G} = -\mathbf{F}^*$ , we obtain the following system of ordinary differential equations:

$$\frac{d\boldsymbol{\varphi}}{dt} = \mathbf{H}\boldsymbol{\varphi}, \tag{12}$$

where  $\mathbf{H} = \mathbf{V}^*\mathbf{J}\mathbf{V}$  is a square matrix of order  $3n + 1$  for  $\alpha = \gamma = 0$  and of order  $3n$  otherwise. A detailed justification of this type of reduction for linear differential–algebraic systems is given in Nechepurenko (2012). To compute the column of amplitude values  $(u_{\alpha\gamma}, v_{\alpha\gamma}, w_{\alpha\gamma}, T_{\alpha\gamma})$  of a disturbance of the form (5), it is necessary to make the following reverse change of variables:

$$(\mathbf{u}^T, \mathbf{v}^T, \mathbf{w}^T, \mathbf{T}^T)^T = \mathbf{E}^{-1/2}\mathbf{V}\boldsymbol{\varphi}. \tag{13}$$

An arbitrary solution to the reduced system (12) can be represented as

$$\boldsymbol{\varphi}(t) = \exp\{t\mathbf{H}\}\boldsymbol{\varphi}^0.$$

Due to the unitary invariance of the second norm,  $\|\mathbf{q}(t)\|_2^2 = \|\boldsymbol{\varphi}(t)\|_2^2$  is a discrete analogue of the total energy density of the corresponding disturbance of the form (5). Therefore, up to the approximation error we have:

$$\Gamma^{\alpha\gamma}(t) = \|\exp\{t\mathbf{H}\}\|_2^2, \quad \Gamma_{\max}^{\alpha\gamma} = \max_{t \geq 0} \Gamma^{\alpha\gamma}(t). \tag{14}$$

Thus, the computation of the maximum amplification  $\Gamma_{\max}^{\alpha\gamma}$  of the total energy density of a disturbance is reduced to the computation of  $t = t_{\text{opt}}^{\alpha\gamma}$  which gives the maximum of  $\Gamma^{\alpha\gamma}(t)$  for  $t \geq 0$ , with  $\mathbf{H}$  being a given square complex matrix. To solve this problem with a given relative accuracy, we use the efficient algorithm (Nechepurenko and Sadkane 2011) based on low-rank approximation. After  $t_{\text{opt}}^{\alpha\gamma}$  is found, we compute the largest singular value  $\sigma_{\text{opt}}$  and the corresponding right  $\boldsymbol{\varphi}_{\text{opt}}$  and left  $\boldsymbol{\psi}_{\text{opt}}$  normalized singular vectors of  $\exp\{t_{\text{opt}}^{\alpha\gamma}\mathbf{H}\}$ . The maximum amplification  $\Gamma_{\max}^{\alpha\gamma}$  is equal to  $\sigma_{\text{opt}}^2$ , and the normalized amplitude of the optimal disturbance at  $t = 0$  and  $t = t_{\text{opt}}^{\alpha\gamma}$  can be computed by using (13) with  $\boldsymbol{\varphi} = \boldsymbol{\varphi}_{\text{opt}}$  and  $\boldsymbol{\varphi} = \boldsymbol{\psi}_{\text{opt}}$ , respectively.

For the results presented below we use the grid with  $n = 100$  internal nodes. It has been verified that further increase in  $n$  does not change the results.

### 3 Large-Scale Structures

#### 3.1 Streamwise-Elongated and Inclined Vortical Structures

We consider a turbulent stratified plane Couette flow at fixed Reynolds number  $Re = 4 \times 10^4$  and two different values of the Richardson number  $Ri = 0.01$  and  $Ri = 0.03$  corresponding to near neutral and stable stratification, respectively. At  $Ri = 0.01$  large-scale streamwise-elongated vortices are observed in the DNS data (Mortikov et al. 2019) against the background

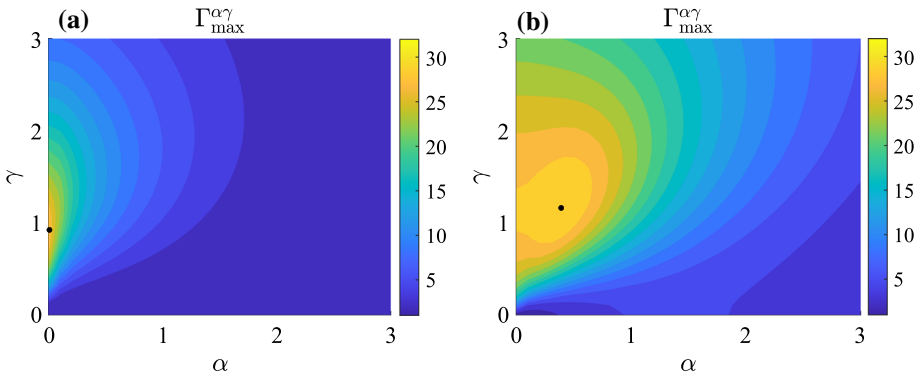


**Fig. 3** Contour lines of the maximum energy amplification  $\Gamma_{\max}^{\alpha\gamma}$  at  $Re = 4 \times 10^4$ ,  $Ri = 0.01$  (a) and  $Re = 4 \times 10^4$ ,  $Ri = 0.03$  (b) in the plane of wavenumbers  $(\alpha, \gamma)$ . The maximum values are marked with black dots

of small-scale turbulence. At  $Ri = 0.03$  large-scale inclined layered structure in the temperature field is observed in numerical simulation (Glazunov et al. 2019).

Figure 3 shows the contour lines of the maximum amplification  $\Gamma_{\max}^{\alpha\gamma}$  of the disturbance total energy density in the first quarter of the plane  $(\alpha, \gamma)$ . It can be seen that at  $Ri = 0.01$  global maximum amplification is achieved with zero streamwise wavenumber and non-zero spanwise wavenumber, i.e. the optimal disturbance is streamwise-elongated, while at  $Ri = 0.03$  it is achieved with non-zero values of both wavenumbers.

The spatial configurations of the optimal disturbances are shown in Fig. 4, where  $u, v, w$ , and  $T$  denote the real parts of the velocity and temperature components of the disturbance of the form (5). Figure 4a–d shows the velocity and temperature fields of optimal disturbance at  $Re = 4 \times 10^4$  and  $Ri = 0.01$  in the plane  $x = 0$  for one spanwise period of the disturbance. The streamwise and spanwise wavenumbers of this optimal disturbance are  $\alpha_{\text{opt}} = 0$  and  $\gamma_{\text{opt}} \approx 0.92$  (spanwise wavelength  $\lambda_z = 2\pi/\gamma_{\text{opt}} \approx 6.8$ ). Here the optimal disturbance resembles large-scale vortices alternating in the direction of rotation. At the initial time  $t = 0$  the vortices are strongly swirled (i.e., the  $(w, v)$  velocity components prevail) and represent rolls. A feature of rolls in a stably stratified flow (in contrast to a neutrally stratified one) is that their temperature is not constant and concentrates mainly near the channel walls. The optimal disturbance at time  $t = t_{\text{opt}}$  represents streaks, i.e. large-scale streamwise-elongated structures with a predominance of the streamwise motion. The streak temperature at the moment of the maximum energy growth is distributed in the same way as the streamwise velocity component. For neutrally stratified flows, rolls develop into streaks via the lift-up effect. This effect also determines the disturbance energy growth at low Richardson numbers. It should be noted that spanwise wavelength of the rolls in the presence of stratification can be larger than the values ( $\lambda_z \approx 4 - 6$ ) obtained in Pujals et al. (2009), Cossu et al. (2009), Hwang and Cossu (2009), where only neutrally stratified turbulent flows were considered.

Figure 4e–h shows velocity and temperature of the optimal disturbance at  $Re = 4 \times 10^4$  and  $Ri = 0.03$  in the plane  $x = 0$  for one spanwise period of the disturbance. The streamwise and spanwise wavenumbers of this disturbance are  $\alpha_{\text{opt}} \approx 0.39$  (streamwise wavelength  $\lambda_x = 2\pi/\alpha_{\text{opt}} \approx 16$ ) and  $\gamma_{\text{opt}} \approx 1.16$  (spanwise wavelength  $\lambda_z = 2\pi/\gamma_{\text{opt}} \approx 5.4$ ). The optimal disturbance shape in the streamwise section of the channel ( $z = 0$ ) differs only in a larger horizontal size. Streamwise velocity and temperature of the optimal disturbance at time  $t = 0$  are strongly inclined with respect to the velocity shear. During disturbance evolution

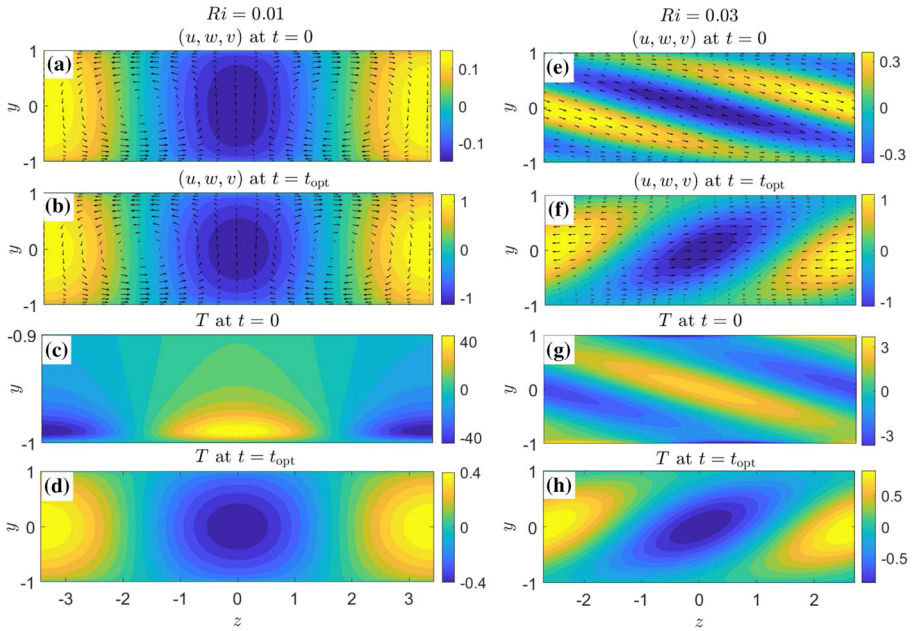


**Fig. 4** Real parts of the optimal disturbance components at  $Re = 4 \times 10^4$ ,  $Ri = 0.01$  (a-d) and at  $Re = 4 \times 10^4$ ,  $Ri = 0.03$  (e-h) in the channel cross-section  $x = 0$ . Isolines of  $u$  (in colour) and velocity field  $(w, v)$  (by arrows) at  $t = 0$  (a, e) and at  $t = t_{opt}$  (b, f). Isolines of  $T$  (in colour) at  $t = 0$  (c, g) and at  $t = t_{opt}$  (d, h). c shows only a part of the channel near the bottom wall

by the time  $t = t_{opt}$ , they develop the opposite slope inherent to the structures formed in the DNS (Zasko et al. 2020). Similar inclined structures were observed in the study of optimal disturbances of the laminar neutrally stratified Couette flow (Butler and Farrell 1992). They require a much shorter time to develop fully than the evolution time of rolls into streaks. The mechanism of the energy growth of such structures was explained by a coupled action of the lift-up effect and the Orr mechanism, which is that the disturbance can gain energy from the main flow while turning with respect to the velocity shear. However, in contrast to the turbulent stratified flow considered here, the inclined structures were a global optimal disturbance in Butler and Farrell (1992) only at low Reynolds numbers and had a much larger streamwise wavelength  $\lambda_x > 41.9$ .

In Fig. 5 the velocity components of the real part of the optimal disturbance (at  $Re = 4 \times 10^4$  and  $Ri = 0.03$ ) are shown in the horizontal section  $y = 0$ . At time  $t = 0$  the horizontal velocity is almost perpendicular to the wavefront, and at  $t = t_{opt}$  is directed along it. Iso-surfaces of the real part of temperature of this optimal disturbance at time  $t = t_{opt}$  are shown in Fig. 6a. Thus, according to Figs. 4, 5, 6, the inclined optimal disturbances resemble rolls (at  $t = 0$ ) and streaks (at  $t = t_{opt}$ ) angled both to the main flow in the horizontal section and to the velocity shear.

Note that  $\Gamma_{max}^{\alpha\gamma} = \Gamma_{max}^{-\alpha,\gamma} = \Gamma_{max}^{\alpha,-\gamma}$ . So if the global maximum energy amplification is achieved with wavenumbers  $(\alpha_{opt}, \gamma_{opt})$ , then there are disturbances of the form (5) with wavenumbers  $(-\alpha_{opt}, \gamma_{opt})$  and  $(\alpha_{opt}, -\gamma_{opt})$  which correspond with the same energy growth. Due to the orthogonality of disturbances of the form (5) for different pairs of the wavenumbers and the linearity of the problem, an arbitrary linear combination of optimal disturbances with

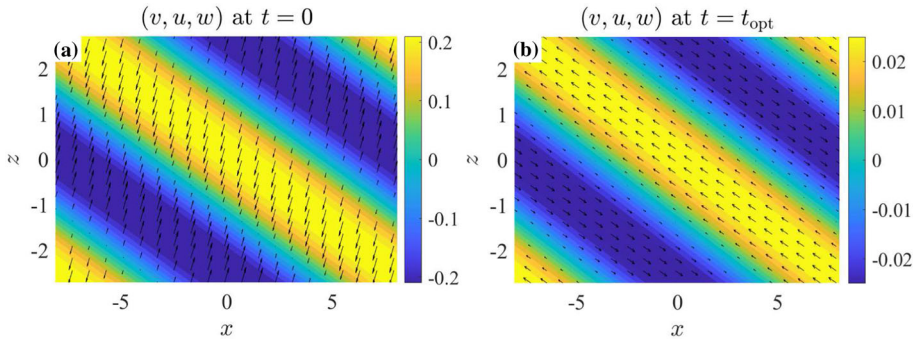


**Fig. 5** Isolines of  $v$  (in colour) and velocity field  $(u, w)$  (by arrows) of the real part of the optimal disturbance at  $Re = 4 \times 10^4$ ,  $Ri = 0.03$  at  $t = 0$  (a) and at  $t = t_{opt}$  (b) in the horizontal section of the channel  $y = 0$

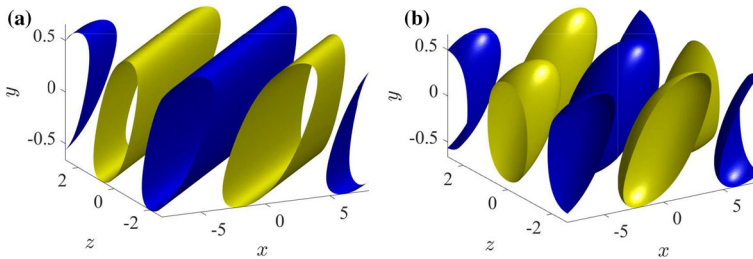


**Fig. 6** Isosurfaces of  $T$  of the optimal disturbances at  $Re = 4 \times 10^4$ ,  $Ri = 0.03$  and time  $t = t_{opt}$ . **a** Real part of the disturbance with wavenumbers  $(\alpha_{opt}, \gamma_{opt})$ . **b** Real part of the sum of disturbances with wavenumbers  $(\alpha_{opt}, \gamma_{opt})$  and  $(\alpha_{opt}, -\gamma_{opt})$

positive and negative spanwise wavenumbers also reaches the maximum energy growth. As an example of such linear combination, Fig. 6b shows the real part of the sum of two above-mentioned optimal disturbances. This disturbance has inclined vortical structure and resemble the structures extracted from the LES data of stably stratified Ekman flow in Sullivan et al. (2016) by conditional averaging methods. In Sullivan et al. (2016) the spatial configuration of the extracted structures was associated with the hairpin vortices. Figure 6b shows that similar vortical structure could be obtained if the large-scale structures are the inclined streaks, since positive and negative spanwise wavenumbers are not distinguished with the conditional averaging used.

Note that Figs. 3 and 4 are similar to some figures in Zasko et al. (2020). We present and discuss them here for better understanding of further results.

### 3.2 Dependence on Reynolds and Richardson Numbers

We consider a turbulent stratified plane Couette flow at 27 different pairs of Reynolds and Richardson numbers ( $Re, Ri$ ) which are varied as follows:  $Re \times 10^{-4} = 1, 2, 4, 6$  and  $0 \leq Ri \leq 0.055$ . The results of computing the global maximum energy amplification  $\Gamma_{max}$ , the optimal wavenumbers  $(\alpha_{opt}, \gamma_{opt})$ , and the optimal time  $t_{opt}$  are given in Table 1. This table also shows the corresponding values of the stability parameter  $\zeta$ .

It is clear from Table 1 that in the case of neutral stratification ( $Ri = 0$ ) the global maximum energy amplification  $\Gamma_{max}$  and the optimal spanwise wavenumber  $\gamma_{opt}$  decrease

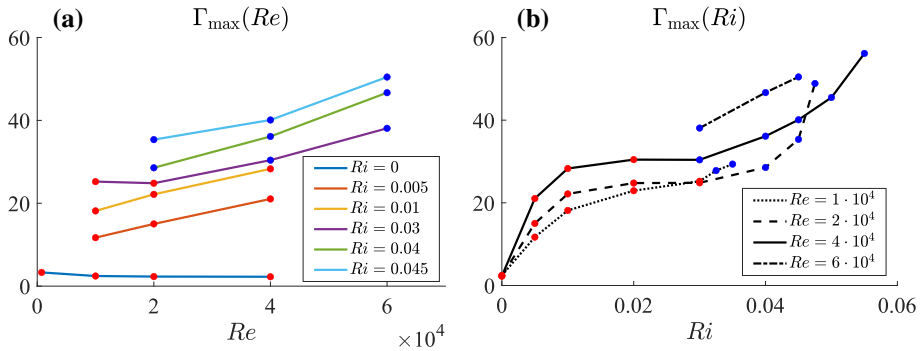


**Fig. 7** Dependence of the global maximum energy amplification  $\Gamma_{\max}$  on  $Re$  for a fixed  $Ri$  (a) and on  $Ri$  for a fixed  $Re$  (b). The values for which  $\alpha_{\text{opt}} = 0$  and  $\alpha_{\text{opt}} > 0$  are marked in red and blue, respectively

with increasing Reynolds number, and the values of  $\Gamma_{\max}$  lie in the range of 2 – 3, which is consistent with results of Hwang and Cossu (2009). The optimal spanwise wavenumber  $\gamma_{\text{opt}}$  at  $Ri = 0$  turns out to be in good agreement with the spanwise size of the large-scale streamwise streaks, which is obtained in the recent DNS (Lee and Moser 2018).

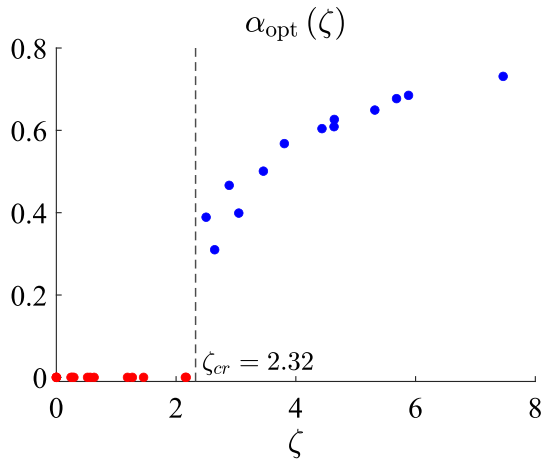
The presence of stable stratification ( $Ri > 0$ ) leads to a significant growth in the global maximum energy amplification. It rises with increasing Reynolds number, which is shown in Fig. 7a. The dependence of the global maximum energy amplification on Richardson number is shown in Fig. 7b. Three characteristic regions are observed on the  $\Gamma_{\max}(Ri)$  curve: growth of the amplification for rolls (red dots), transition from rolls to inclined structures, and growth of the amplification for inclined structures (blue dots). It might seem counter-intuitive that maximum energy amplification increases with increasing Richardson number but the following detail should be taken into account: an increase in  $Ri$  leads to a decrease in the eddy viscosity and in the eddy diffusivity (see Fig. 2).

Note that in the DNS of turbulent neutrally stratified plane Couette flow the most intense large-scale motions are rolls and streaks, while during transition to stable stratification a sharp weakening of all large-scale fluctuations is observed. Therefore, small values of global maximum energy amplification at  $Ri = 0$  are most likely related with the significant contribution of the discussed large-scale structures to eddy viscosity that was noted in Sect. 1.

Dependence of the optimal streamwise wavenumber on the stability parameter  $\zeta$  is shown in Fig. 8. Optimal streamwise wavenumber increases for more stable conditions, with the clear critical value  $\zeta_{\text{cr}} \approx 2.32$  being observed, such that for  $\zeta < \zeta_{\text{cr}}$  the optimal disturbance represents large-scale streamwise rolls developing into streamwise streaks, while for  $\zeta > \zeta_{\text{cr}}$  the optimal disturbance represents inclined structures with non-zero streamwise wavenumber. The considered range of  $\zeta$  corresponds to the values measured in the stable atmospheric boundary layer, e.g.,  $\zeta_{\text{cr}} = 2.32$  corresponds to  $\zeta = 0.81$  if the definition of the Obukhov length scale includes additional multiplicative factor  $1/\kappa$  with  $\kappa = 0.35$  as in Businger et al. (1971).

A lack of DNS data near the critical value  $\zeta_{\text{cr}}$  does not allow to make strict conclusions, but we suppose that the transition from  $\alpha_{\text{opt}} = 0$  to  $\alpha_{\text{opt}} > 0$  is smooth, since the dependence of  $\Gamma_{\max}^{\alpha\gamma}$  on wavenumbers always has only one local maximum in the large-scale part of the  $(\alpha, \gamma)$  plane (that is seen in Fig. 3 and similar figures at other considered  $(Re, Ri)$  pairs). The another argument is that the optimal disturbances with  $\alpha_{\text{opt}} > 0$  resemble inclined rolls

**Fig. 8** Dependence of the optimal streamwise wavenumber  $\alpha_{\text{opt}}$  on the stability parameter  $\zeta$ , according to the data from Table 1. Zero and positive values of  $\alpha_{\text{opt}}$  are marked in red and blue, respectively



and streaks, i.e. one can suppose the smooth transition of the disturbance form from the case  $\alpha_{\text{opt}} = 0$ , when the optimal disturbances are streamwise-elongated rolls and streaks.

### 4 Physical Mechanisms of the Optimal Disturbance Growth

#### 4.1 Influence of Buoyancy Forces

The question we intend to answer is: whether the non-zero streamwise wavenumber of the optimal disturbance of a stably stratified turbulent flow is a result of the shape of turbulent main flow velocity  $\bar{U}(y)$  and eddy viscosity  $\bar{\nu}(y)$  profiles, or it is non-zero due to the influence of the buoyancy forces? For this purpose, we compute the optimal disturbances with buoyancy force excluded, using the same main flow velocity  $\bar{U}(y)$  and eddy viscosity  $\bar{\nu}(y)$ . The optimal disturbances of the form (5) are computed assuming  $Ri = 0$  in equation for the disturbance amplitudes (6) and in the functional (7), which in this case represents only the disturbance kinetic energy. We consider values of Richardson number  $Ri \geq 0.03$ , where the optimal streamwise wavenumber is non-zero. In order to clarify the influence of the shape of  $\bar{U}(y)$  and  $\bar{\nu}(y)$  profiles, the results are compared with a further simplified problem — neutrally stratified laminar Couette flow. Since for stable stratification the velocity profile  $\bar{U}(y)$  in the channel centre is close to linear one, we choose the following parameters to describe a laminar flow: viscosity  $\bar{\nu}(0)$  and wall velocities  $\pm\tilde{U}/2$ , where:

$$\tilde{U} = 2 \frac{d\bar{U}}{dy}(0)h. \tag{15}$$

For a pair of parameters  $(Ri, Re)$ , we define the effective Reynolds number  $Re_* = \tilde{U}h/\bar{\nu}(0)$  and compare three types of the optimal disturbances: including buoyancy forces (data from Table 1), excluding buoyancy forces, and those found for laminar flow. Figure 9 shows the dependence of the global maximum energy amplification  $\Gamma_{\text{max}}$  and optimal streamwise wavenumber  $\alpha_{\text{opt}}$  on the effective Reynolds number for these three types of optimal disturbances. The data from Butler and Farrell (1992) for laminar flow is also shown on Fig. 9 for additional verification of our numerical technology.



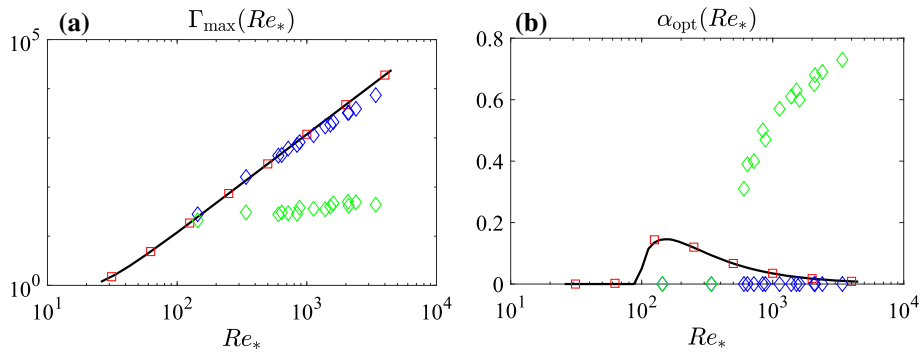


**Fig. 9** The global maximum energy amplification  $\Gamma_{\max}$  (a) and optimal streamwise wavenumber  $\alpha_{\text{opt}}$  (b) as functions of effective Reynolds number  $Re_*$  for laminar Couette flow (black — our computations, red — data from Butler and Farrell (1992)) and for turbulent flow (green — including buoyancy forces, blue — excluding them)

The global maximum energy amplifications for the disturbances computed for the turbulent and laminar velocity profiles with buoyancy excluded are close to each other and are 1-2 orders of magnitude greater than the values obtained with the buoyancy forces being taken into account. When the buoyancy forces are excluded, the optimal disturbances of the turbulent flow have exactly zero streamwise wavenumber, contrary to complicated dependence of streamwise number on the effective Reynolds number in the laminar case. Thus, we conclude that the non-zero optimal streamwise wavenumber cannot be explained by only the shape of the turbulent main flow velocity  $\bar{U}(y)$  and eddy viscosity  $\bar{\nu}(y)$  profiles and are associated with the influence of the buoyancy forces (see Fig. 9b).

### 4.2 Lift-Up Effect and Orr Mechanism

There are two mechanisms of the disturbance kinetic energy growth, particularly, the lift-up effect and the inviscid Orr mechanism. In order to separate the action of these mechanisms on the disturbances of the form (5) with non-zero wavenumbers  $\alpha$  and  $\gamma$ , we rotate the coordinate system in the plane  $(x, z)$  by the angle  $\theta = \arcsin(\alpha/\gamma')$  in clockwise direction, where  $\gamma' = \sqrt{\alpha^2 + \gamma^2}$ . The new horizontal coordinates  $x' = x \cos \theta - z \sin \theta$  and  $z' = x \sin \theta + z \cos \theta$  are directed along and perpendicular to the wavefront, respectively (see Fig. 5). The main flow velocity in the rotated coordinate system has non-zero streamwise  $\bar{U}' = \bar{U} \cos \theta$  and spanwise  $\bar{W}' = \bar{U} \sin \theta$  components, and velocity components of the disturbance in these directions are  $u'_{\alpha\gamma} = u_{\alpha\gamma} \cos \theta - w_{\alpha\gamma} \sin \theta$  and  $w'_{\alpha\gamma} = u_{\alpha\gamma} \sin \theta + w_{\alpha\gamma} \cos \theta$ , respectively. In the new coordinates, the disturbance (5) is written in the form:

$$(u'_{\alpha\gamma}, v_{\alpha\gamma}, w'_{\alpha\gamma}, p_{\alpha\gamma}, T_{\alpha\gamma})e^{i\gamma'z'}, \tag{16}$$

and governing equations of its amplitude evolution are as follows:

$$\begin{aligned} \frac{\partial u'_{\alpha\gamma}}{\partial t} + i\gamma'\bar{W}'u'_{\alpha\gamma} + \frac{d\bar{U}'}{dy}v_{\alpha\gamma} - \Delta_v^{\alpha\gamma}u'_{\alpha\gamma} &= 0, \\ \frac{\partial v_{\alpha\gamma}}{\partial t} + i\gamma'\bar{W}'v_{\alpha\gamma} + \frac{\partial p_{\alpha\gamma}}{\partial y} - \Delta_v^{\alpha\gamma}v_{\alpha\gamma} - RiT_{\alpha\gamma} &= 0, \end{aligned}$$

$$\begin{aligned} \frac{\partial w'_{\alpha\gamma}}{\partial t} + i\gamma'\bar{W}'w'_{\alpha\gamma} + \frac{d\bar{W}'}{dy}v_{\alpha\gamma} + i\gamma'p_{\alpha\gamma} - \Delta_v^{\alpha\gamma}w'_{\alpha\gamma} &= 0, \\ \frac{\partial T_{\alpha\gamma}}{\partial t} + i\gamma'\bar{W}'T_{\alpha\gamma} + \frac{d\bar{T}}{dy}v_{\alpha\gamma} - \Delta_\mu^{\alpha\gamma}T_{\alpha\gamma} &= 0, \\ \frac{\partial v_{\alpha\gamma}}{\partial y} + i\gamma'w'_{\alpha\gamma} &= 0. \end{aligned}$$

Note that the last four equations of (17) do not include the variable  $u'_{\alpha\gamma}$ , i.e. these equations form a complete system of equations describing the evolution of the other four variables. The evolution of  $u'_{\alpha\gamma}$  is described by the first equation and is uniquely determined by its initial value and the variable  $v_{\alpha\gamma}$ .

From (17) we can derive the evolution equations for the kinetic  $\mathcal{E}_t^K$  and potential  $\mathcal{E}_t^P = \mathcal{E}_t - \mathcal{E}_t^K$  components of the total energy density for disturbance of the form (16):

$$\begin{aligned} \frac{d\mathcal{E}_t^K}{dt} &= - \underbrace{\int_{-1}^1 \frac{d\bar{U}'}{dy} \operatorname{Re}\{v_{\alpha\gamma}u'^*_{\alpha\gamma}\} dy}_{\text{lift-up term}} - \underbrace{\int_{-1}^1 \frac{d\bar{W}'}{dy} \operatorname{Re}\{v_{\alpha\gamma}w'^*_{\alpha\gamma}\} dy}_{\text{Orr term}} \\ &\quad + \underbrace{Ri \int_{-1}^1 \operatorname{Re}\{T_{\alpha\gamma}v^*_{\alpha\gamma}\} dy}_{\text{buoyancy term}} \\ &\quad - \underbrace{\int_{-1}^1 \bar{v}[\gamma'^2 (|u'_{\alpha\gamma}|^2 + |v_{\alpha\gamma}|^2 + |w'_{\alpha\gamma}|^2) + \left|\frac{\partial u'_{\alpha\gamma}}{\partial y}\right|^2 + \left|\frac{\partial v_{\alpha\gamma}}{\partial y}\right|^2 + \left|\frac{\partial w'_{\alpha\gamma}}{\partial y}\right|^2] dy}_{\text{kinetic energy dissipation term}}, \end{aligned} \tag{17}$$

$$\frac{d\mathcal{E}_t^P}{dt} = -Ri \int_{-1}^1 \operatorname{Re}\{T_{\alpha\gamma}v^*_{\alpha\gamma}\} dy - Ri \underbrace{\int_{-1}^1 \frac{\bar{\mu}}{d\bar{T}/dy} (\gamma'^2 |T_{\alpha\gamma}|^2 + \left|\frac{\partial T_{\alpha\gamma}}{\partial y}\right|^2) dy}_{\text{potential energy dissipation term}}. \tag{18}$$

Time dependences of  $\mathcal{E}_t^K$ ,  $\mathcal{E}_t^P$ , and the contribution of the underlined terms in (17) and (18) are shown in Fig. 10 for two typical regimes, i.e. at  $Re = 4 \times 10^4$  and  $Ri = 0.01$  (weak stratification, rolls and streaks) and at  $Re = 4 \times 10^4$  and  $Ri = 0.055$  (strong stable stratification, inclined structures).

The first two terms on the right-hand side (r.h.s.) of (17) are responsible for production of the disturbance Kinetic energy due to the lift-up effect and due to the Orr mechanism, respectively. If  $\cos\theta \neq 0$ , the lift-up effect can increase the disturbance kinetic energy along  $x'$  due to the vertical transport of the main streamwise velocity  $\bar{U}'$ . If  $\sin\theta \neq 0$ , the Orr mechanism can increase the kinetic energy of vortical motion in plane  $(y, z')$ , which is accompanied by rotation of closed circulations by the shear of the main flow.

The sum of the third term on the r.h.s. of (17) and the first one on the r.h.s. of (18) is equal to zero and represents the fact that the buoyancy term does not change the total energy of the disturbance and is only responsible for the conversion between potential energy and kinetic energy.

In Fig. 10c the energy cycle of the optimal disturbance with zero streamwise wavenumber is shown. Although the redistribution of energy between the potential and kinetic components through the buoyancy conversion term is relatively small, it is due to this term the energy cycle is similar to the energy cycle of the internal gravity wave: velocity fluctuations deform the temperature isosurfaces and this leads to the accumulation of the potential energy of the fluctuations. During the release of the potential energy, the rolls are spinning up in the opposite direction. Consequently, the contribution of the lift-up effect periodically changes the sign with an approximate period of  $2t_{opt}$ . The time moment, at which the first change in the direction of rotation occurs, is close to  $t_{opt}$ . At this moment all the kinetic energy is contained in the streaks. Since the vertical spatial scale of such disturbance does not vary much in time, the moment of maximum kinetic energy dissipation is also close to  $t_{opt}$ . The internal gravity wave mechanism limits the time during which an optimal disturbance can develop. As a consequence, the maximum energy amplification also decreases in comparison (see Fig. 9) with the case described in the previous section, where the buoyancy forces are excluded. Let us estimate the optimal time  $t_{opt}$ , using the frequency of the internal gravity wave (Brunt–Väisälä frequency) at the channel centre:

$$N = \sqrt{Ri \frac{d\bar{T}}{dy}}(0). \tag{19}$$

The time  $t_{opt}$  accounts for approximately the half-period of the energy cycle, which corresponds to a quarter of the wave period. The channel height (vertical wavenumber  $k_y = \pi$ ) is taken as the characteristic vertical scale of the wave. Then the estimate is as follows:

$$t_{opt}^* = \frac{\pi}{2\omega}, \quad \omega = N \sqrt{\frac{\alpha^2 + \gamma^2}{\alpha^2 + \gamma^2 + \pi^2}}. \tag{20}$$

For  $Re = 4 \times 10^4$ ,  $Ri = 0.01$  and  $Re = 4 \times 10^4$ ,  $Ri = 0.055$ , the optimal times are  $t_{opt} = 131$  and  $t_{opt} = 43.8$ , respectively, while the estimate gives the following values:  $t_{opt}^* = 138.2$  and  $t_{opt}^* = 29.9$ . Note that this estimate is more accurate for optimal disturbances with zero streamwise wavenumber, but gives only crude approximation of  $t_{opt}$  for inclined structures since  $k_y$  depends on time.

With an increase in Richardson number, the Brunt–Väisälä frequency increases, and, as a consequence, the corresponding characteristic time decreases. From Fig. 10d it follows that for the strongest stability considered ( $Ri = 0.055$ ), the contribution of buoyancy to the energy cycle increases significantly in comparison with  $Ri = 0.01$ . The Orr mechanism, which is possible only for the disturbances with a non-zero streamwise wavenumber, turns out to be beneficial from the energetic point-of-view on short time periods. Inclined structures are destroyed by the shear of the main flow with the formation of large vertical gradients, and as a result the energy cycle completes only one period, in contrast to the disturbances with zero streamwise wavenumber. The time moment of the maximum kinetic energy dissipation shifts from the optimal time  $t_{opt}$  to a later time ( $\approx 1.5t_{opt}$ ) when the large vertical gradients are formed. Note that the energy growth of the optimal disturbances for the considered range of Richardson number occurs mainly due to the lift-up effect.

It should be emphasized that the dissipation of the kinetic energy is small during the development of the inclined structures. This means that the results should depend weakly on the choice of the eddy viscosity operator. As shown by additional computations not presented in this work, the energy cycle of the inclined structures (see Fig. 10d) is not very sensitive to decrease or increase in the coefficients of eddy viscosity and eddy diffusivity.

In the linear model (6), the developing optimal disturbance does not contribute to the mean profiles, since it is harmonic in streamwise and spanwise directions. However, it can lead to spatial inhomogeneity of flow characteristics even in the linear model. We further consider the evolution of the optimal disturbance against the background of the mean flow:

$$(\tilde{u}, \tilde{v}, \tilde{w}, \tilde{T}) = (\bar{U}(y), 0, 0, \bar{T}(y)) + \epsilon \text{Re}\{(u_t, v_t, w_t, T_t)e^{i\alpha_{\text{opt}}x + i\gamma_{\text{opt}}z}\}, \tag{21}$$

in the linear model (6), where  $\epsilon$  is the constant factor, and  $u_t, v_t, w_t, T_t$  are time-dependent amplitudes of the developing optimal disturbance, which is normalized to have unit energy density at  $t = 0$ . The stratification of the mean flow is described by the gradient Richardson number:

$$Ri_g = Ri \frac{d\bar{T}/dy}{(d\bar{U}/dy)^2}, \tag{22}$$

and one can define the contribution to the gradient Richardson number from the developing optimal disturbance as follows:

$$\tilde{Ri}_g = Ri \frac{\partial \tilde{T} / \partial y}{(\partial \tilde{u} / \partial y)^2} - Ri_g. \tag{23}$$

The quantity  $\tilde{Ri}_g$  evolves in time with the optimal disturbance development. Figure 11 shows  $\tilde{Ri}_g$  for the inclined optimal disturbance at  $Re = 4 \times 10^4$ ,  $Ri = 0.055$  at the optimal time moment  $t = t_{\text{opt}}$  (a) and the time moment  $t = 1.5t_{\text{opt}}$  (b), which is close to the moment of maximum kinetic energy dissipation (see Fig. 10d). The constant factor  $\epsilon$  is taken as  $\epsilon^2 = 3 \times 10^{-6}$ , which corresponds to 1% of mean total energy of the turbulent fluctuations in the DNS. The mean profile  $Ri_g$  is nearly constant near the channel centre and equals to 0.17 (Glazunov et al. 2019). The contribution of the optimal disturbance is rather high (up to 20% from the maximum value of  $Ri_g$ ) especially at  $t = 1.5t_{\text{opt}}$  although the disturbance energy density at that moment is less than at  $t_{\text{opt}}$ . Thus, the development of the inclined optimal disturbance can lead to spatial inhomogeneity of flow stratification after reaching the optimal time moment. The same effect was observed in (Kaminski et al. 2017), where the laminar stably stratified shear flow was considered. In the fully developed turbulent flow (in the DNS) this can lead to the appearance of the large-scale inclined temperature fronts.

### 5 Near-Wall Structures

In the previous works on the study of optimal disturbances of the turbulent Poiseuille flow (del Alamo and Jimenez 2006; Pujals et al. 2009) and turbulent boundary layer with zero external pressure gradient (Cossu et al. 2009), it was established that in addition to the global maximum in wavenumbers  $\alpha$  and  $\gamma$ , the maximum energy amplification  $\Gamma_{\text{max}}^{\alpha\gamma}$  also has a local maximum, which is attained for zero streamwise wavenumber and sufficiently large spanwise wavenumber. In these works the optimal disturbance corresponding to this local maximum was associated with organized structures in the form of near-wall streamwise rolls developing into near-wall streamwise streaks which extend through the viscous and buffer layers. No local maximum was found in the study of optimal disturbances of turbulent plane Couette flow (Hwang and Cossu 2010). A possible reason for this, as the authors noted, is insufficiently high Reynolds number considered.

The local maximum corresponds to the near-wall structures and it is suitable to use the following dimensionless spatial coordinates for its analysis:  $y_+ = Re_\tau(y + 1)$ ,  $z_+ = Re_\tau z$ ,

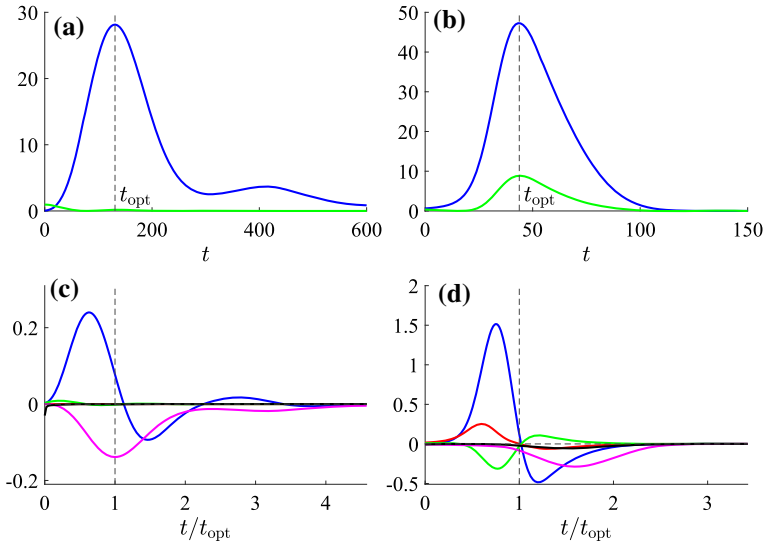
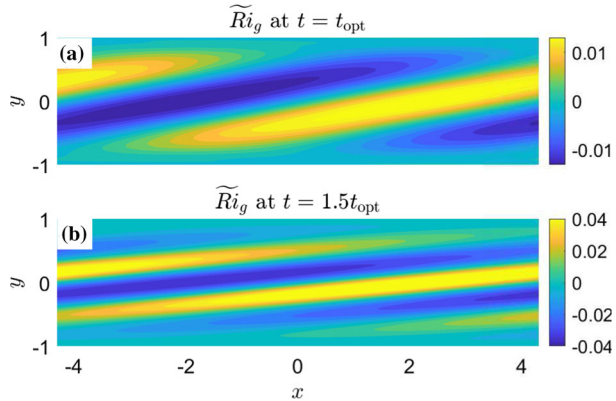


**Fig. 10** **a, b** Evolution of kinetic energy (blue) and potential energy (green) of the optimal disturbances. **c, d** Contributions of individual terms of equations (17) and (18) to the energy change rate, namely, lift-up term (blue), Orr term (red), buoyancy term (green), kinetic energy dissipation (pink) and potential energy dissipation (black).  $Re = 4 \times 10^4$ ,  $Ri = 0.01$  (**a, c**) and  $Re = 4 \times 10^4$ ,  $Ri = 0.055$  (**b, d**)

**Fig. 11** The anomaly in gradient Richardson number  $\widetilde{Ri}_g$  in the streamwise section of the channel ( $z = 0$ ) for the optimal disturbance at  $Re = 4 \times 10^4$  and  $Ri = 0.055$  at the optimal time moment  $t = t_{opt}$  (**a**) and at the time moment  $t = 1.5t_{opt}$  (**b**)



$\gamma_+ = \gamma / Re_\tau$ . The values of friction Reynolds number  $Re_\tau$  for all considered pairs of  $(Re, Ri)$  are presented in Table 1. Note that the new wall-normal coordinate  $y_+$  is shifted to satisfy  $y_+ = 0$  on the bottom channel wall.

Figure 12a shows the dependence of the maximum energy amplification  $\Gamma_{max}^{\alpha\gamma}$  on the spanwise wavenumber  $\gamma$  ranged from 0.1 to 1000 at several values of the streamwise wavenumber at  $Re = 4 \times 10^4$  and  $Ri = 0.02$ . It is evident that the flow has local maximum of energy amplification which weakly depends on the streamwise wavenumber. This is consistent with the previous findings in del Alamo and Jimenez (2006), Pujals et al. (2009) and Cossu et al. (2009) for neutrally stratified flows. Note that at neutral stratification local maximum was also observed. The values of spanwise wavenumber, optimal disturbance development time, and maximum energy amplification corresponding to this maximum are denoted by  $\tilde{\gamma}_{opt}$ ,  $\tilde{t}_{opt}$

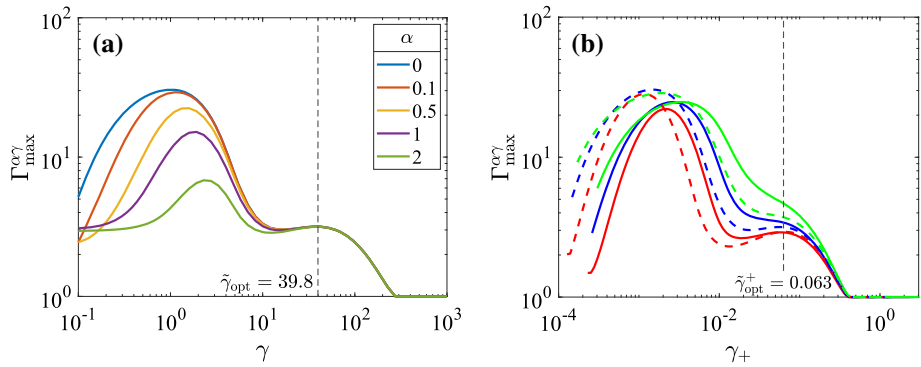


**Fig. 12** **a** Dependence of the maximum energy amplification  $\Gamma_{\max}^{\alpha\gamma}$  on the spanwise wavenumber  $\gamma$  at various values of the streamwise wavenumber  $\alpha$  at  $Re = 4 \times 10^4$  and  $Ri = 0.02$ . **b** Dependence of the maximum energy amplification  $\Gamma_{\max}^{\alpha\gamma}$  on the spanwise wavenumber  $\gamma_+$  in wall units at  $\alpha = 0$  and  $Re = 2 \times 10^4$  (solid),  $Re = 4 \times 10^4$  (dotted) and  $Ri = 0.01$  (red),  $Ri = 0.02$  (blue), and  $Ri = 0.03$  (green)

and  $\tilde{\Gamma}_{\max}$ , respectively. These characteristics, computed for various values of Reynolds and Richardson numbers, are presented in Table 1.

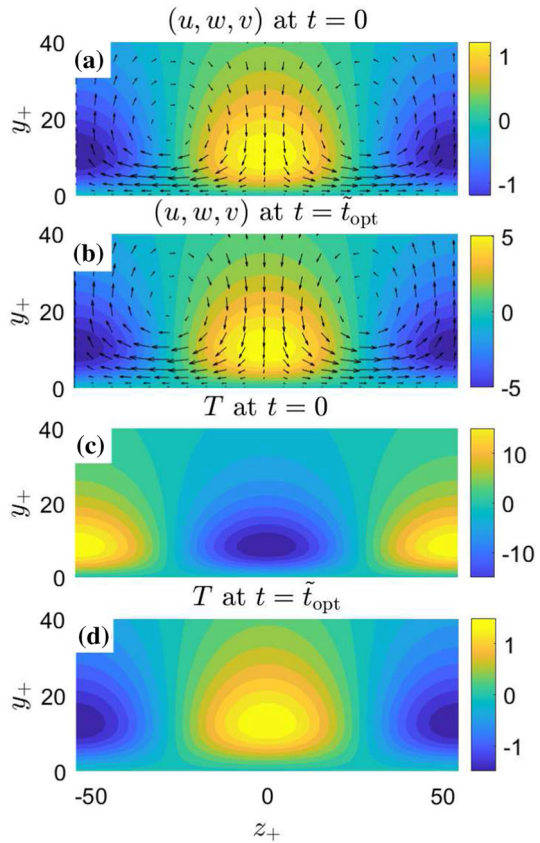
Although spanwise wavenumber  $\tilde{\gamma}_{\text{opt}}$  varies strongly with the change in Reynolds and Richardson numbers, it remains almost constant in wall units, namely,  $\tilde{\gamma}_{\text{opt}}^+ = \tilde{\gamma}_{\text{opt}}/Re_\tau \approx 0.063$ . This is illustrated by Fig. 12b, which shows the dependence of maximum energy amplification at  $\alpha = 0$  on the spanwise wavenumber in wall units  $\gamma_+$ . Note that the local maximum becomes less pronounced with an increase in the Richardson number. If local maximum is not found for some particular pair of Reynolds and Richardson numbers, we define  $\tilde{\Gamma}_{\max}$  as the maximum energy amplification at  $\alpha = 0$  and  $\gamma_+ = 0.063$ , assuming that the spanwise size of near-wall structures remains constant. Thus, the spanwise size of the optimal disturbances corresponding to the local maximum (if it exists) of maximum energy amplification equals  $\lambda_z^+ = 2\pi/\tilde{\gamma}_{\text{opt}}^+ \approx 100$  in wall units and does not depend on Reynolds and Richardson numbers under weak stratification. These results are consistent with findings for neutrally stratified turbulent flows.

Real parts of the velocity and temperature components of the optimal disturbance corresponding to the local maximum  $\tilde{\Gamma}_{\max}$  at  $Re = 4 \times 10^4$ ,  $Ri = 0.01$  in the channel cross-section  $x = 0$  are shown in Fig. 13. This optimal disturbance has zero streamwise wavenumber and spanwise wavenumber  $\tilde{\gamma}_{\text{opt}} = 53$ . This optimal disturbance is represented by near-wall streamwise-elongated structures with typical vertical size  $y_+ \approx 40$ . At  $t = 0$  the kinetic energy of wall-normal and spanwise motions and the potential energy prevail, i.e. the optimal disturbance represents near-wall rolls. By the time  $t = \tilde{t}_{\text{opt}}$ , the kinetic energy of streamwise motion tends to prevail, i.e. they are near-wall streaks. Note that the optimal disturbance temperature and streamwise velocity are similar in shape. The main physical mechanism responsible for the development of near-wall optimal disturbances is the lift-up effect.

The dependence of the local maximum  $\tilde{\Gamma}_{\max}$  on Richardson number for different Reynolds numbers is shown in Fig. 14a. A significant (greater than linear) growth of the maximum energy amplification is observed with the increase in the Richardson number. Thus, the presence of stratification has slight effect on the spatial configuration of the near-wall optimal disturbances but strongly influences their energy amplification. Note that under neutral stratification  $\tilde{\Gamma}_{\max}$  does not depend on Reynolds number, which is consistent with the following



**Fig. 13** Real parts of the near-wall optimal disturbance components at  $Re = 4 \times 10^4$ ,  $Ri = 0.01$  in the section  $x = 0$  near the bottom wall. Isolines of  $u$  (in colour) and field  $(w, v)$  (by arrows) at  $t = 0$  (a) and at  $t = \tilde{t}_{opt}$  (b). Isolines of  $T$  (in colour) at  $t = 0$  (c) and at  $t = \tilde{t}_{opt}$  (d)



works del Alamo and Jimenez (2006), Pujals et al. (2009), Cossu et al. (2009), and only with increase in Richardson number this dependence is apparent.

However, the variance of near-wall streamwise velocity fluctuations in the DNS (Glazunov et al. 2019) decreases with increasing Richardson number (Fig. 14b) in contrast to  $\tilde{\Gamma}_{max}(Ri)$  (Fig. 14a). This discrepancy can occur since large-scale structures appearing under neutral and weak stratification in a turbulent flow make a significant contribution to the momentum flux which enters the definition of the eddy viscosity coefficient. Since the near-wall optimal disturbances develop only via the lift-up effect, the eddy viscosity plays a decisive role for the value of energy amplification because the energy cycle of the near-wall structures is similar to that presented in Fig. 10c. The more contribution of the near-wall structures to the near-wall turbulent flow, the more eddy viscosity, and, as a consequence, the less energy amplification of optimal disturbances in the linear model. It should be emphasized that similar reasoning is not applicable to large-scale inclined optimal disturbances under stable stratification, since the kinetic energy dissipation is small during their development (see Fig. 10d).

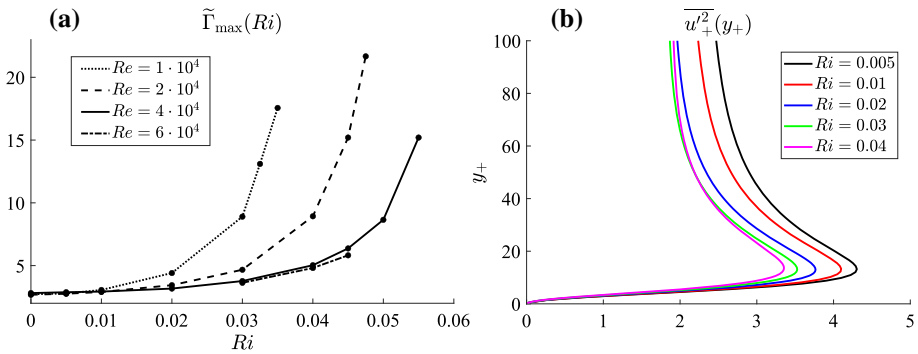


**Fig. 14** **a** Dependence of the local maximum  $\tilde{\Gamma}_{\max}$  of maximum energy amplification on  $Ri$  at various  $Re$ . **b** The variance of the streamwise velocity fluctuations in wall units, at  $Re = 4 \times 10^4$  and various  $Ri$ , obtained from the DNS (Glazunov et al. 2019)

## 6 Summary

Optimal disturbances of a turbulent stably stratified plane Couette flow were computed in a wide range of the Reynolds and Richardson numbers. The effects due to the presence of stable stratification were studied and highlighted. The following results were obtained:

- (1) Under neutral and weakly stable conditions, the optimal disturbances correspond to streamwise rolls evolving into streamwise streaks. In the presence of even a weak stratification, the maximum energy amplification of these disturbances increases significantly compared to neutral stratification. The latter property might be associated with a shortcoming in the formulation of a simplified problem, since the observed large-scale structures under neutral stratification significantly contribute to the momentum flux, i.e. the eddy viscosity obtained with this flux might be overestimated. We notice that in the DNS under neutral stratification, large structures resembling rolls and streaks permanently exist, while they are significantly weakened at any non-zero positive values of the Richardson number.
- (2) With an increase in Richardson number, the type of optimal disturbances changes. They become vortical structures with a non-zero streamwise wavenumber, inclined in vertical cross-section against the mean velocity shear, and change their inclination to the opposite in the process of evolution. At the moment of maximum energy amplification, these disturbances also resemble streaky structures turned with respect to the main flow in the horizontal plane.
- (3) The transition between two types of optimal disturbances does not show a clear dependence on the external flow parameters, i.e. the Reynolds and Richardson numbers. It was found that a convenient parameter characterizing the transition from streamwise streaks to turned streaks (inclined structures) is the dimensionless stability parameter  $\zeta = h/L$ , where  $L$  is the Obukhov length scale. The transition occurs at the value  $\zeta_{\text{cr}} \approx 2.32$ . The indirect relation between spatial characteristics of optimal disturbances to  $Re$  and  $Ri$  and the existence of universal dependence on  $\zeta$  suggests that the near-wall effects do not have a decisive influence on these disturbances at large  $Re$ .
- (4) It was shown that the emergence of optimal disturbances with a non-zero optimal streamwise wavenumber is directly associated with the influence of buoyancy forces and cannot be explained by the shape of mean velocity and eddy viscosity profiles.

- (5) The energy growth time of inclined structures does not vary much ( $t_{\text{opt}} \approx 40$ ) with increase in Richardson number and turned out to be shorter than the evolution time of rolls into streaks.
- (6) The energy growth of inclined structures is associated with the coupled action of the lift-up effect and the Orr mechanism. The contribution from the lift-up effect is decisive in all cases, but the role of the Orr mechanism increases with an increase in the Richardson number.
- (7) It was shown that under stable stratification the disturbance growth time  $t_{\text{opt}}$  is related to the period of the internal gravity wave with the same horizontal wave numbers. The optimal time  $t_{\text{opt}}$  for both streamwise structures and inclined structures is approximately a quarter of the wave period.
- (8) The dissipation of the kinetic energy is small during the development of the inclined structures. This means that the results should depend weakly on the choice of the eddy viscosity operator.
- (9) The maximum of the kinetic energy dissipation of inclined structures occurs later than the optimal growth time, i.e. it occurs at the moment when the structures are more inclined in the vertical plane. Note that such dissipation is a parametrization of non-linear mechanism of generating small-scale turbulence by the inclined structures. With sufficient disturbance energy, this generation can locally increase the eddy viscosity and eddy diffusivity coefficients (which are prescribed in the considered problem). This can lead to spatially inhomogeneous mixing of the mean velocity and temperature profiles. It can be assumed that it is precisely this non-linear mechanism that leads to the appearance of well-mixed layers separated by fronts in the temperature fields. This hypothesis should be verified on the basis of ensemble computations with DNS or LES of high spatial resolution.
- (10) The dependence of the maximum energy amplification on wavenumbers has a local maximum, in addition to the global one, corresponding to the near-wall rolls developing into the near-wall streaks. These structures have a universal spanwise size (about 100 wall length units). The dimensionless size of the near-wall structures and their shape are weakly dependent on the Richardson number. Computation of linear optimal disturbances predicts an increase in their energy growth with increasing Richardson number. This effect is not supported by the DNS data, where the streamwise velocity variance decreases with increasing in Richardson number. Most likely, this contradiction is also associated with the simplifications used and, in particular, the inapplicability of the diffusion approximation to structure–turbulence interactions in the buffer sublayer.

**Acknowledgements** Numerical analysis of the optimal disturbances and mathematical justification of the results were supported by Russian Science Foundation (Grant No. 17-71-20149). Direct numerical simulation and physical justification of the results were supported by Russian Foundation for Basic Research (Grant No. 20-05-00776). Direct numerical simulations were carried out using the equipment of the shared research facilities of HPC computing resources at Lomonosov Moscow State University. We express our gratitude to the two anonymous reviewers for their helpful comments and suggestions.

**Data availability** The results of DNS used during the current study are available from E.V. Mortikov (evgeny.mortikov@gmail.com) on reasonable request.

## Declarations

**Conflicts of interest** Authors declare no conflict of interest.

## References

- Adrian RJ (2007) Hairpin vortex organization in wall turbulence. *Phys Fluids* 19(4):041,301
- Bakewell HP Jr, Lumley JL (1967) Viscous sublayer and adjacent wall region in turbulent pipe flow. *Phys Fluids* 10(9):1880–1889
- Boiko AV, Dovgal AV, Grek GR, Kozlov VV (2011) Physics of transitional shear flows: instability and laminar–turbulent transition in incompressible near-wall shear layers. Springer Science & Business Media, Berlin
- Brandt L (2014) The lift-up effect: the linear mechanism behind transition and turbulence in shear flows. *Eur J Mech B/Fluids* 47:80–96
- Businger JA, Wyngaard JC, Izumi Y, Bradley EF (1971) Flux-profile relationships in the atmospheric surface layer. *J Atmos Sci* 28(2):181–189
- Butler KM, Farrell BF (1992) Three-dimensional optimal perturbations in viscous shear flow. *Phys Fluids* 4(8):1637–1650
- Canuto C, Hussaini MY, Quarteroni A, Zang TA (2007) Spectral methods: fundamentals in single domains. Springer Science & Business Media, Berlin
- Cossu C, Hwang Y (2017) Self-sustaining processes at all scales in wall-bounded turbulent shear flows. *Phil Trans R Soc* 375(2089):20160,088
- Cossu C, Pujals G, Depardon S (2009) Optimal transient growth and very large-scale structures in turbulent boundary layers. *J Fluid Mech* 619:79–94
- del Alamo JC, Jimenez J (2006) Linear energy amplification in turbulent channels. *J Fluid Mech* 559:205–213
- Ellingsen T, Palm E (1975) Stability of linear flow. *Phys Fluids* 18(4):487–488
- Foster RC (1997) Structure and energetics of optimal ekman layer perturbations. *J Fluid Mech* 333:97–123
- Glazunov AV (2014) Numerical simulation of stably stratified turbulent flows over flat and urban surfaces. *Izv Atmos Ocean Phys* 50(3):236–245
- Glazunov AV, Mortikov EV, Barskov KV, Kadantsev EV, Zilitinkevich SS (2019) Layered structure of stably stratified turbulent shear flows. *Izv Atmos Ocean Phys* 55(4):312–323
- Hamilton JM, Kim J, Waleffe F (1995) Regeneration mechanisms of near-wall turbulence structures. *J Fluid Mech* 287(1):317–348
- Homemma S, Adrian R (2003) Packet structure of surface eddies in the atmospheric boundary layer. *Boundary-Layer Meteorol* 106(1):147–170
- Hwang Y, Cossu C (2009) Optimal amplification of large-scale structures in plane turbulent couette flow. In: Sixth international symposium on turbulence and shear flow phenomena, pp 159–164
- Hwang Y, Cossu C (2010) Amplification of coherent streaks in the turbulent couette flow: an input-output analysis at low reynolds number. *J Fluid Mech* 643:333–348
- Jiao Y, Hwang Y, Chernyshenko SI (2021) The orr mechanism in transition of parallel shear flow. *Phys Rev Fluids* 6(2):023–902
- Kaminski AK, Caulfield CP, Taylor JR (2014) Transient growth in strongly stratified shear layers. *J Fluid Mech* 758:R4-1-R4-12
- Kaminski AK, Caulfield CP, Taylor JR (2017) Nonlinear evolution of linear optimal perturbations of strongly stratified shear layers. *J Fluid Mech* 825:213–244
- Kitoh O, Nakabayashi K, Nishimura F (2005) Experimental study on mean velocity and turbulence characteristics of plane couette flow: low-reynolds-number effects and large longitudinal vortical structure. *J Fluid Mech* 539:199–227
- Kline SJ, Reynolds WC, Schraub FA, Runstadler PW (1967) The structure of turbulent boundary layers. *J Fluid Mech* 30(4):741–773
- Komminaho J, Lundbladh A, Johansson AV (1996) Very large structures in plane turbulent couette flow. *J Fluid Mech* 320:259–285
- Landahl MT (1980) A note on an algebraic instability of inviscid parallel shear flows. *J Fluid Mech* 98(2):243–251
- Lee M, Moser D (2018) Extreme-scale motions in turbulent plane couette flows. *J Fluid Mech* 842:128–145
- Lee MJ, Kim J (1991) The structure of turbulence in a simulated plane couette flow. Eighth Symp. Turbulent Shear Flows 5:5.3.1-5.3.6
- Lorenz EN (1955) Available potential energy and the maintenance of the general circulation. *Tellus* 7(2):157–167
- Malkus WVR (1956) Outline of a theory of turbulent shear flow. *J Fluid Mech* 1(5):521–539
- McKeon BJ (2017) The engine behind (wall) turbulence: perspectives on scale interactions. *J Fluid Mech* 817:1–86
- Moin P, Kim J (1982) Numerical investigation of turbulent channel flow. *J Fluid Mech* 118:341–377
- Monin AS, Obukhov AM (1954) Basic laws of turbulent mixing in the surface layer of the atmosphere. *Contrib Geophys Inst Acad Sci USSR* 151(163):e187

- Mortikov EV, Glazunov AV, Lykosov VN (2019) Numerical study of plane couette flow: turbulence statistics and the structure of pressure-strain correlations. *Russ J Numer Anal Math Model* 34(2):119–132
- Nechepurenko YM (2012) On the dimension reduction of linear differential-algebraic control systems. *Doklady Math* 86(1):457–459
- Nechepurenko YM, Sadkane M (2011) A low-rank approximation for computing the matrix exponential norm. *SIAM J Matr Anal Appl* 32(2):349–363
- Obukhov AM (1971) Turbulence in an atmosphere with a non-uniform temperature. *Boundary-Layer Meteorol* 2(1):7–29
- Orr WMF (1907) The stability or instability of the steady motions of a perfect liquid and of a viscous liquid. part i: A perfect liquid. In: *Proceedings of the Royal Irish Academy. Section A: Mathematical and Physical Sciences*, vol 27, pp 9–68
- Petenko I, Argentini S, Casasanta G, Genthon C, Kallistratova M (2019) Stable surface-based turbulent layer during the polar winter at dome c, antarctica: Sodar and in situ observations. *Boundary-Layer Meteorol* 171(1):101–128
- Pujals G, García-Villalba M, Cossu C, Depardon S (2009) A note on optimal transient growth in turbulent channel flows. *Phys Fluids* 21(1):015–109
- Rawat S, Cossu C, Hwang Y, Rincon F (2015) On the self-sustained nature of large-scale motions in turbulent couette flow. *J Fluid Mech* 782:515–540
- Reddy SC, Henningson DS (1993) Energy growth in viscous channel flows. *J Fluid Mech* 252:209–238
- Reynolds WC, Hussain AKMF (1972) The mechanics of an organized wave in turbulent shear flow. part 3. theoretical models and comparisons with experiments. *J Fluid Mech* 54(2):263–288
- Schmid PJ (2007) Nonmodal stability theory. *Annu Rev Fluid Mech* 39:129–162
- Schmid PJ, Henningson DS (1994) Optimal energy density growth in hagen-poiseuille flow. *J Fluid Mech* 277:197–225
- Schmid PJ, Henningson DS (2001) *Stability and Transition in Shear Flows*. Springer-Verlag, New York
- Smith CR, Metzler SP (1983) The characteristics of low-speed streaks in the near-wall region of a turbulent boundary layer. *J Fluid Mech* 129(1):27–54
- Sullivan PP, Weil JC, Patton EG, Jonker HJ, Mironov DV (2016) Turbulent winds and temperature fronts in large-eddy simulations of the stable atmospheric boundary layer. *J Atmos Sci* 73(4):1815–1840
- Waleffe F (1997) On a self-sustaining process in shear flows. *Phys Fluids* 9(4):883–900
- Zasko GV, Nechepurenko YM (2021) Spectral analysis of the optimal disturbances of stratified turbulent couette flow. *Comp Math Math Phys* 61(1):136–149
- Zasko GV, Glazunov AV, Mortikov EV, Nechepurenko YM (2020) Large-scale structures in stratified turbulent couette flow and optimal disturbances. *Russ J Numer Anal Math Model* 35(1):37–53
- Zilitinkevich SS, Elperin T, Kleeorin N, Rogachevskii I (2007) Energy-and flux-budget (efb) turbulence closure model for stably stratified flows. part i: Steady-state, homogeneous regimes. In: *Atmospheric Boundary Layers*, Springer, pp 11–35
- Zilitinkevich SS, Elperin T, Kleeorin N, Rogachevskii I, Esau I (2013) A hierarchy of energy-and flux-budget (efb) turbulence closure models for stably-stratified geophysical flows. *Boundary-Layer Meteorol* 146(3):341–373

**Publisher's Note** Springer Nature remains neutral with regard to jurisdictional claims in published maps and institutional affiliations.

Springer Nature or its licensor holds exclusive rights to this article under a publishing agreement with the author(s) or other rightsholder(s); author self-archiving of the accepted manuscript version of this article is solely governed by the terms of such publishing agreement and applicable law.